Research Square

Preprints are preliminary reports that have not undergone peer review.
They should not be considered conclusive, used to inform clinical practice,
or referenced by the media as validated information.

Prodrug-Engineered PI3K/mTOR Nanoblockers Enable Coordinated Tumor Control and Allograft Protection after Transplantation

Ning Wang
First Affiliated Hospital Zhejiang University
Yang Fu
First Affiliated Hospital Zhejiang University
Xinyu Tong
First Affiliated Hospital Zhejiang University
Hong Tang
First Affiliated Hospital Zhejiang University
Ke Zhou
First Affiliated Hospital Zhejiang University
Zhonghan Wu
First Affiliated Hospital Zhejiang University
Hyon-Seung Yi
First Affiliated Hospital Zhejiang University
Rong Su
First Affiliated Hospital Zhejiang University
Jintao Zheng
First Affiliated Hospital Zhejiang University
Jiaming Wang
First Affiliated Hospital Zhejiang University
Wentao Zhao
First Affiliated Hospital Zhejiang University
Ruiqi Sun
First Affiliated Hospital Zhejiang University
Zhi Liang
First Affiliated Hospital Zhejiang University
Shusen Zheng
First Affiliated Hospital Zhejiang University
Zhentao Yang
First Affiliated Hospital Zhejiang University

Haiyang Xie

xiehy@zju.edu.cn

First Affiliated Hospital Zhejiang University

Research Article

Keywords: Prodrug engineering, Drug delivery, Organ transplantation, Tumor recurrence

Posted Date: November 9th, 2026

DOI: https://doi.org/10.21203/rs.3.rs-11346380/v1

License: This work is licensed under a Creative Commons Attribution 4.0 International License.
Read Full License

Additional Declarations: No competing interests reported.

Prodrug-Engineered PI3K/mTOR Nanoblockers Enable Coordinated Tumor Control and Allograft Protection after Transplantation

Ning Wang[a, b, #], Yang Fu[c, #], Xinyu Tong[a, b, #], Hong Tang[a, b], Ke Zhou[c], Zhonghan Wu[c], Hyon-Seung Yi[d], Rong Su[a, b], Jintao Zheng[a, b], Jiaming Wang[a, b], Wentao Zhao[a, b], Ruiqi Sun[a, b], Zhi Liang[a, b], Shusen Zheng*[a, b], Zhentao Yang*[e], Haiyang Xie*[a, b]

[a]Division of Hepatobiliary and Pancreatic Surgery, Department of Surgery, The First Affiliated Hospital, Zhejiang University School of Medicine, Hangzhou 310003, China

[b]NHC Key Laboratory of Combined Multi-organ Transplantation, Key Laboratory of Organ Transplantation, Zhejiang Province. Institute of Organ Transplantation, Zhejiang University. State Key Laboratory for Diagnosis and Treatment of Infectious Diseases, National Clinical Research Center for Infectious Diseases, Hangzhou 310003, China

[c]Division of Lung Transplantation and Thoracic Surgery, Department of Surgery, The First Affiliated Hospital, Zhejiang University School of Medicine, Hangzhou 310003, China

[d]Division of Endocrinology and Metabolism, Department of Internal Medicine, Chungnam National University School of Medicine, Daejeon 35015, Korea

[e]Division of Thoracic Surgery, The First Affiliated Hospital, Zhejiang University School of Medicine, Hangzhou, 310003, China

#These authors contributed equally to this work.

*Corresponding author. E-mail: xiehy@zju.edu.cn, E-mail: 21718116@zju.edu.cn, Email: shusenzheng@zju.edu.cn.

Abstract

Organ transplant recipients with malignancies require therapeutic strategies that control tumor progression without compromising allograft protection. Although mTOR inhibition provides a clinically validated strategy for balancing immunosuppression and tumor control after transplantation, compensatory PI3K/Akt activation limits durable efficacy. Dual PI3K/mTOR blockade represents a rational solution, yet its therapeutic potential is restricted by suboptimal pharmacological properties, including insufficient tissue exposure and dose-limiting toxicity, which compromise sustained target engagement. Here, we

developed a prodrug-enabled nanoliposomal platform (PMIProsome) for sustained dual PI3K/mTOR inhibition by converting PF-04691502, a representative dual PI3K/mTOR inhibitor, into a disulfide-linked cholesterol prodrug. PMIProsome optimized systemic drug exposure by enhancing tumor accumulation and reducing systemic toxicity, enabling sustained PI3K/Akt/mTOR pathway inhibition and durable tumor control in an orthotopic hepatocellular carcinoma model. Beyond tumor suppression, PMIProsome retained immunomodulatory activity by attenuating cytotoxic T-cell activation and inflammatory responses, thereby promoting allograft survival. In a concomitant tumor-allograft model, PMIProsome achieved simultaneous tumor control and allograft protection, overcoming the therapeutic conflict between antitumor efficacy and immunosuppression after transplantation. Collectively, these findings establish prodrug-engineered PI3K/mTOR nanoblockers as a therapeutic strategy for coordinating tumor control and allograft protection after transplantation.

Keywords: Prodrug engineering, Drug delivery, Organ transplantation, Tumor recurrence

1. Introduction

Organ transplantation in patients with a history of malignancy presents a distinctive therapeutic conflict [1]. Long-term immunosuppression is indispensable for allograft protection, yet excessive suppression of immune surveillance may facilitate tumor recurrence or progression [2]. Conversely, many antitumor therapies depend on immune activation and may therefore compromise allograft tolerance [3]. This challenge is particularly evident in liver transplantation for hepatocellular carcinoma (HCC) [2, 4], in which transplantation removes both the tumor and the diseased liver but does not eliminate the risk of postoperative recurrence. Current approaches largely rely on balancing immunosuppressive intensity with oncological risk, yet this strategy provides limited control over the divergent biological processes governing graft tolerance and tumor progression. Among current immunosuppressive agents, inhibitors of the mechanistic target of rapamycin (mTOR) are uniquely attractive because their immunosuppressive effects are accompanied by direct inhibition of tumor-cell growth and metabolism [5-7].

Rapamycin and its analogues predominantly suppress mTOR complex 1 (mTORC1), thereby inhibiting lymphocyte proliferation and tumor-cell growth [8, 9]. However, selective mTORC1 inhibition provides incomplete control of the PI3K/Akt/mTOR (PAM) signaling network [10]. Relief of mTORC1-dependent negative feedback can reactivate upstream PI3K/Akt signaling [11, 12], while persistent mTORC2 activity sustains Akt phosphorylation and cell survival [13]. These adaptive responses have been associated with reduced treatment durability and acquired resistance in multiple cancers, including HCC [12, 14]. Dual PI3K/mTOR inhibitors were developed to overcome these limitations by simultaneously targeting class I PI3K and the catalytic activity of mTORC1/2 [10, 15]. This broader pathway blockade can suppress both oncogenic signaling and immune-cell activation, creating a unique pharmacological opportunity to simultaneously achieve tumor control and allograft protection. Nevertheless, the expanded pathway coverage required for dual PI3K/mTOR inhibition creates a challenge in balancing therapeutic efficacy with controlled drug exposure.

Clinical translation of dual PI3K/mTOR inhibitors has been limited by dose-limiting toxicity, suboptimal systemic disposition, and insufficient maintenance of pathway inhibition at pathological sites [16-18]. These limitations are particularly consequential in transplantation, where excessive systemic inhibition may aggravate immune and metabolic toxicity [19, 20], whereas insufficient tissue exposure may allow rapid pathway reactivation and tumor progression. The therapeutic value of dual PI3K/mTOR inhibition therefore depends not only on inhibitor potency, but also on precise control of drug distribution, retention, and release [16, 21]. Nanocarriers can improve aqueous dispersibility and alter tissue exposure [22]; however, conventional liposomal encapsulation of hydrophobic kinase inhibitors is often limited by poor drug-lipid compatibility, unstable loading, premature leakage, and formulation heterogeneity [23, 24]. Prodrug engineering integrated with nanocarrier design offers a potential solution by embedding the drug within the carrier architecture and coupling systemic transport with stimulus-responsive release [25, 26].

Here, we developed PMIProsome by integrating a cholesterol-modified, disulfide-linked prodrug of PF-04691502 into PEGylated nanoliposomes (**Fig. 1A**). This design was intended to improve drug-lipid compatibility and formulation integrity during systemic transport, while enabling reduction-triggered release of the active inhibitor under glutathione-rich conditions. We hypothesized that coupling prodrug engineering with nanoliposomal delivery would enhance drug exposure at pathological sites and prolong PI3K/mTOR pathway suppression without increasing systemic toxicity. Accordingly, we evaluated the formulation characteristics, release behavior, biodistribution, safety, and therapeutic efficacy of PMIProsome in HCC, allogeneic transplantation, and concomitant tumor-allograft models. (**Fig. 1B**). Collectively, this work provides a prodrug-engineered PI3K/mTOR nanoblocker platform for harnessing dual PI3K/mTOR inhibition to address the competing demands of tumor control and allograft protection.

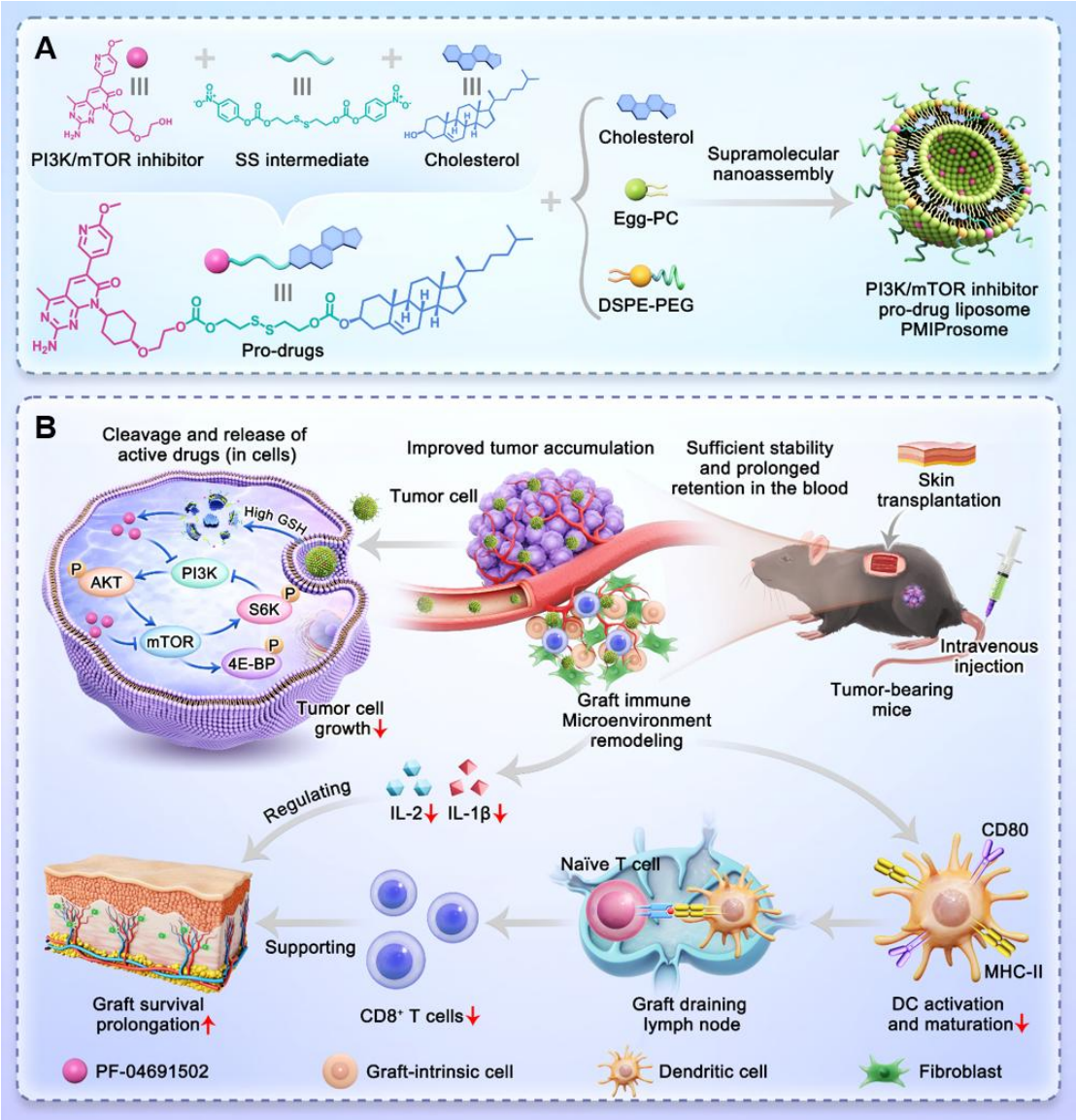


Fig.1. Schematic illustration of the design and therapeutic mechanism of the PI3K/mTOR inhibitor prodrug nanoliposomal platform (PMIProsome). (A) A redox-responsive PF-04691502 prodrug was engineered through conjugation with a disulfide-containing self-immolative spacer and cholesterol moiety, followed by supramolecular assembly with phospholipids and DSPE-PEG to form stable PEGylated nanoliposomes for systemic delivery. (B) PMIProsome achieved prolonged circulation, enhanced tumor accumulation, and glutathione-responsive drug release, enabling effective PI3K/Akt/mTOR pathway blockade and suppression of compensatory signaling activation. Meanwhile, PMIProsome simultaneously exerted antitumor and immunosuppressive effects by inhibiting tumor growth, dendritic cell maturation, $CD8^+$ T-cell activation, and inflammatory cytokine production, thereby prolonging allograft survival.

2. Methods and materials

2.1. Animals

C57BL/6 (6-week-old male) and BALB/c (6-week-old male) mice were purchased from Hangzhou Medical College and housed in the Experimental Animal Center of the First Affiliated Hospital, Zhejiang University School of Medicine; all animal experiments were conducted following approval by the Institutional Animal Care and Ethics Committee of the hospital (approval number: 2025-190).

2.2. Cell lines and cell culture

Human HCC cell lines Huh7 (RRID: CVCL_0336), HCCLM3 (RRID: CVCL_6832), and SNU-449 (RRID: CVCL_0454) were obtained from the Cell Bank of the Chinese Academy of Sciences. Huh7-derived Rapa-resistant cells (Huh7-R) were kindly provided by Professor Xiao Xu's laboratory at Zhejiang University. The acquisition of rapamycin resistance was confirmed by CCK-8 assays showing reduced rapamycin sensitivity compared with parental Huh7 cells (Huh7-N) [27]. Murine HCC cell lines Hepa1-6 (RRID: CVCL_0327) and Hepatoma-22 (RRID: CVCL_H613) were purchased from the National Infrastructure of Cell Line Resources. Hepatoma-22 cells were cultured in RPMI-1640 medium (PM150110, Procell) supplemented with 10% fetal bovine serum (FBS, A5256801, Gibco), while all other cell lines were maintained in DMEM (PM150210, Procell) with 10% FBS, all under standard conditions of 37°C and 5% CO_2.

2.3. Preparation and characterization of liposomal PI3K/mTOR inhibitor

The synthesis of the PI3K/mTOR inhibitor (PF-04691502, HY-15177, MCE) prodrug was described in detail in supplementary materials, and its chemical structure was confirmed by ^1H nuclear magnetic resonance (NMR). PF-04691502 (PF) pro-drug liposomes (PMIProsome) were prepared by diluting lipids and PF in a 19:1 (w/w) ratio. The lipids, composed of egg phosphatidylcholine (HY-125854, MCE), cholesterol (HY-N0322R, MCE), and 1,2-distearoyl-sn-glycero-3-phosphoethanolamine-N-poly (ethylene glycol)$_{2000}$ at a 7:2:1 mass ratio, were dissolved in 0.9 mL of anhydrous ethanol. Subsequently, 0.1 mL of DMSO containing the PF prodrug (10 mg/mL, equivalent to PF) was added. The mixture was injected into 9 mL of PBS and subjected to ultracentrifugation to remove precipitates,

resulting in stable PMIProsmoe (PF equivalent concentration of 1 mg/mL). Drug concentration was determined using high-performance liquid chromatography (HPLC) with absorbance detection at 256 nm. Liposome morphology, size distribution, and dispersity were evaluated by transmission electron microscopy (TEM) and dynamic light scattering (DLS).

For evaluation of the redox-responsive behavior of the PF prodrug, the prodrug was placed into a dialysis bag (molecular weight cutoff 7000 Da) and immersed in release medium containing 10 mM dithiothreitol (DTT, 20311ES60, Yeasen). At predetermined time points, aliquots of the external medium were withdrawn and analyzed by HPLC to determine the amount of released PF. To further assess the stimulus-responsive release performance of PMIProsome, the liposomes were similarly loaded into dialysis bags and incubated in release medium either with or without 10 mM DTT. At predetermined time intervals, aliquots of the external medium were collected, hydrolyzed with 0.1 M NaOH at 37°C for 4 h, and neutralized with 0.1 M HCl. The released PF amount was subsequently quantified by HPLC with absorbance detection at 256 nm.

2.4. Cell viability and proliferation assay

Cell viability was assessed using the CCK-8 solution (HY-K0301, MCE). Cells were seeded in 96-well plates at 3,000 cells/well density and cultured overnight for adherence. Cells were then exposed to varying concentrations of Rapamycin (Rapa, HY-10219, MCE), PF, or PMIProsome for 48 hours. Following drug treatment, the medium was replaced with a 10% CCK-8 working solution and incubated for 1 hour. Absorbance at 450 nm was measured using a spectrophotometer (Bio-Rad, USA). Relative cell viability was calculated using the standard formula.

Cell proliferation was evaluated using an EdU incorporation assay. Briefly, cells were seeded in 6-well plates at 20,000 cells/well and cultured overnight. Cells were treated with Rapa (2 μM), PF (2 μM), or PMIProsome (2 μM PF-equivalent concentration) for 48 hours. After drug treatment, cells were incubated with 50 μM EdU (C0071L, Beyotime) for 2 hours to label proliferating cells, fixed in 4% formaldehyde for 15 mins, permeabilized with 0.3% Triton X-100 (20107ES20, Yeasen) for 10 mins, and incubated with Alexa Fluor® 488 for 30 mins. Nuclei were counterstained with DAPI (C1006, Beyotime) for 10 mins, and

proliferation was evaluated via fluorescence microscopy.

2.5. Colony formation assay

Single-cell suspensions were prepared and seeded into 6-well plates at a density of 3,000 cells per well. Once individual adherent cells developed into macroscopically visible and uniformly distributed granular colonies, the culture medium was replaced with drug-containing medium supplemented with Rapa (2 μM), PF (2 μM), or PMIProsome (equivalent to 2 μM PF), followed by an additional 48 hours of incubation. Following treatment, cells were fixed with methanol for 15 mins, rinsed thoroughly, and stained with crystal violet solution (G1064, Solarbio) under light-protected conditions for 15 mins. After washing, the plates were air-dried in the dark at room temperature, and the resulting colonies were photographed, counted, and subjected to statistical analysis.

2.6. Cell cycle and apoptotic assay

Cells were seeded in 6-well plates at 20,000 cells per well and cultured for 24 hours. To induce serum starvation, the medium was replaced with low-serum medium containing 0.1% fetal bovine serum, followed by 48-hour incubation to synchronize the cell cycle and arrest cells at the G0 phase. After starvation, cells were treated with Rapa (2 μM), PF (2 μM), or PMIProsome (PF-equivalent concentration of 2 μM) in fresh complete medium for an additional 48 hours. Subsequently, cells were harvested and fixed in 75% ethanol overnight at -20°C. Fixed cells were stained with a cell cycle detection reagent (CCS012, Multi Sciences) and incubated in the dark for 30 mins. The relative proportion of cells in each cell cycle phase were analyzed by flow cytometry.

Apoptosis was analyzed by Annexin V-FITC/PI staining (40302ES60, Yeasen) and flow cytometry. Cells were seeded in 6-well plates at 100,000 cells per well and incubated for 24 hours. Cells were then treated with Rapa (2 μM), PF (2 μM), or PMIProsome (PF-equivalent concentration of 2 μM) for 48 hours. After treatment, cells were collected, stained with 5 μL Annexin V-FITC and 5 μL PI in the dark for 10 mins. Apoptosis was analyzed by flow cytometry.

2.7. BMDC maturation and antigen presentation *in vitro*

Bone marrow-derived dendritic cells (BMDCs) were generated from bone marrow cells of C57BL/6 mice by flushing femoral bone marrow and culturing in RPMI-1640 medium

supplemented with 20 ng/mL recombinant murine GM-CSF (RP01206, ABclonal) and 10 ng/mL IL-4 (RP01161, ABclonal). After 2 days of culture, cells were treated with either 200 nM Rapa, 200 nM PF, or 200 nM PMIProsome (PF-equivalent) for an additional 48 hours. Mature BMDCs were induced by adding 0.2 μg/mL LPS for 12 hours. For phenotypic analysis, cells were stained with Zombie NIR™ Fixable Viability Kit (15 min at room temperature, 423106, BioLegend), followed by Fc receptor blocking with anti-CD16/32 antibody (10 min at 4°C, 101319, BioLegend). Surface markers were labeled with antibodies against CD45 (Percp-Cy5.5, 103132, BioLegend), CD11c (FITC, 117306, BioLegend), CD80 (PE-Cy7, 104734, BioLegend), CD86 (APC, 159216, BioLegend), and MHC-II (PE, 107608, BioLegend). Mature BMDCs were defined as $CD45^+CD11c^+$ cells co-expressing $CD80^+CD86^+$ or MHC-II^+. To assess antigen presentation, BMDCs were incubated with 2 μg/mL $OVA_{257-264}$ peptide (SIINFEKL, HY-P1489, MCE) for 24 hours. Antigen presentation was evaluated using PE-conjugated anti-mouse H-$2K^b$/SIINFEKL antibody (141603, BioLegend). OVA-presenting BMDCs were identified as $CD45^+CD11c^+$ cells positive for CD80 and H-2Kb/SIINFEKL.

2.8. T cell proliferation and activation assay

Mouse spleen derived lymphocyte (MSDLs) isolation was performed using lymphocyte separation medium (P8860, Solarbio). Freshly isolated MSDLs were labeled with carboxyfluorescein succinimidyl ester (CFSE, C34570, Invitrogen) for 10 min at 37°C. Cells were exposed to 200 nM Rapa, 200 nM PF, or PMIProsome (equivalent to 200 nM PF) alongside T cell activation stimuli: recombinant murine IL-2 (2 ng/ml, RP01384, ABclonal), anti-CD3 antibody (100340, BioLegend), and anti-CD28 antibody (102116, BioLegend). Co-incubation was maintained for 5 days. After incubation, cells were stained with anti-mouse CD4 (Percp-cy5.5, 100434, BioLegend) and CD8a (APC, 100712, BioLegend) antibodies. T cell proliferation was quantified by measuring CFSE mean fluorescence intensity (MFI) in $CD4^+$ and $CD8^+$ populations via flow cytometry.

For T cell activation analysis, freshly isolated MSLs were first stimulated with recombinant murine IL-2, anti-CD3 antibody, and anti-CD28 antibody for 2 days. Subsequently, activated T cells were treated with a panel of PI3K/mTOR inhibitors (200 nM), including Apitolisib (Api, HY-13246, MCE), Bimiralisib (Bim, HY-12868, MCE), Dactolisib (Dac, HY-

50673, MCE), VS-5584 (VS, HY-16585, MCE), PF-04691502, GDC-0084 (GDC, HY-19962, MCE), GNE-477 (GNE, HY-11042, MCE), Voxtalisib (Vox, HY-15900, MCE), and Rapa, for an additional 2 days. Subsequently, cells were harvested and stained with fluorochrome-conjugated antibodies against mouse CD45 (BV510, 563891, BD Biosciences), CD3e (BV650, 564378, BD Biosciences), CD4 (PE-Cy7, 100422, BioLegend), CD8a (Alexa Fluor 700, 557959, BD Biosciences), perforin (FITC, 154310, BioLegend), granzyme B (PE, 168804, BioLegend), and IFN-γ (APC, 505810, BioLegend). The expression levels of these effector molecules in T cell subpopulations were then analyzed by flow cytometry to evaluate the impact of different PMIs on T cell activation.

2.9. Western blot

SNU-449 cells were treated with Rapa (2 μM), PF (2 μM), or PMIProsome (2 μM PF-equivalent concentration) for 48 hours, followed by lysis with RIPA buffer (89901, Thermo). Cell lysates were separated via SDS-PAGE and transferred to polyvinylidene fluoride (PVDF) membranes. Membranes were blocked, then incubated overnight at 4°C with primary antibodies: phosphorylated mTOR (Ser2448) (D9C2, 5536, CST), mTOR (7C10, 2983, CST), phosphorylated P70 S6 kinase (Thr389) (108D2, 9234, CST), phosphorylated 4EBP1 (Thr37/46) (236B4, 2855, CST), 4EBP1 (53H11, 9644, CST), P70 S6 kinase (E8K6T, 34475, CST), phosphorylated Akt (Ser473) (D9E, 4060, CST), Akt (11E7, 4685, CST), and GAPDH (D16H11, 5174, CST). After primary antibody incubation, membranes were incubated with HRP-conjugated secondary antibodies for 1 hour. Protein expression levels were visualized using ECL Prime Western Blotting Detection Reagent (32209, Thermo).

2.10. qRT-PCR

BMDCs following drug treatment were subjected to RNA extraction using an RNA extraction kit (RK30120, ABclonal), and the purified RNA was reverse-transcribed into cDNA using ABScript Neo RT Master Mix for qPCR with gDNA Remover (RK20433, ABclonal). Subsequent qPCR was performed with 2X Universal SYBR Green Fast qPCR Mix (RK21203, ABclonal), utilizing GAPDH as the internal reference gene to quantify relative expression levels of target genes. Primer sequences for all genes are provided in Table S1.

2.11. Intravital imaging and intratumoral accumulation of nano-liposome

C57BL/6 mice bearing Hepatoma-22 subcutaneous tumors were randomly divided into four groups upon tumor volume reaching ~100 mm^3: (1) Free DiR (HY-D1048, MCE): intraperitoneal (i.p.) injection of DiR, (2) PF^{DiR}: i.p. injection of PF-loaded DiR at 2 mg/kg PF, and (3) $PMIProsome^{DiR}$: intravenous (i.v.) injection of PMIProsome-loaded DiR at 2 mg/kg PF-equivalent concentration. The DiR dosage was uniformly set at 1 mg/kg across all groups. *In vivo* biodistribution was assessed via imaging system (IVIS Lumina LT, Revvity) at designated time points, while *ex vivo* fluorescence intensity of tumors and major organs (heart, liver, spleen, lungs, kidneys, and tumor-draining lymph nodes) was quantified.

To evaluate tumor drug accumulation following systemic administration, mice bearing Hepatoma-22 subcutaneous tumors were treated with PF or PMIProsome as described above. At 12 h and 48 h post-treatment, tumors were excised, weighed, and homogenized in PBS. The homogenates were then hydrolyzed with 0.1 M sodium hydroxide for 4 h, followed by neutralization with 0.1 M hydrochloric acid. After protein precipitation with acetonitrile (34851, Merck), the supernatants were collected and analyzed by HPLC with detection at 256 nm to quantify the accumulated concentration of PF in tumor tissues.

2.12. Biosafety assessment

Healthy C57BL/6 mice were randomly divided into seven groups: (1) Control (untreated), (2-4) PF-treated groups receiving low (2 mg/kg), medium (4 mg/kg), or high (8 mg/kg) doses via i.p. injection, and (5-7) PMIProsome-treated groups receiving low (2 mg/kg), medium (4 mg/kg), or high (8 mg/kg) PF-equivalent doses via i.v. injection. Treatments were administered every other day for three doses. Body weight was monitored throughout the treatment period. On day 5 post-treatment, blood samples were collected for hematological and biochemical analyses, and major organs were processed for histopathological evaluation to assess drug safety. To assess the long-term biosafety of PMIProsome, mice receiving low (2 mg/kg) or high (8 mg/kg) PF-equivalent doses were followed for 30 days after administration. At the endpoint, hematological parameters and serum biochemical markers of liver and kidney function were evaluated.

2.13. Tumor therapy experiments

For the orthotopic Hepa1-6-luc liver tumor model, a suspension of 3×10^5 Hepa1-6-luc cells mixed with Matrigel (354234, Corning) was injected into the left hepatic lobe of C57BL/6 mice. One day post-inoculation, mice were randomly allocated to four groups: Control (untreated), Rapa (2 mg/kg, i.p.), PF (2 mg/kg, i.p.), and PMIProsome (2 mg/kg PF-equivalent, i.v.). Treatments were administered every other day for three doses. Therapeutic efficacy was assessed at designated time points using an IVIS imaging system. Bioluminescence signals from Hepa1-6-luc cells were detected after intraperitoneal injection of D-luciferin potassium salt (C3654, Apexbio), enabling quantitative evaluation of tumor burden and therapeutic response.

2.14. Allogeneic skin transplantation model and immunological evaluation

For the skin transplantation model, BALB/c mice served as donors and C57BL/6 mice as recipients. A 1 cm × 1 cm full-thickness dorsal skin graft bed was created in recipients, followed by transplantation of an equally sized BALB/c skin allograft, sutured in place and protected with a bandage. Postoperatively, mice were randomly assigned to four groups: Control (untreated), Rapa (2 mg/kg, i.p.), PF (2 mg/kg, i.p.), and PMIProsome (2 mg/kg PF-equivalent, i.v.). Treatments were administered every other day for three doses. Allograft survival was monitored daily from day 8 post-transplantation until allograft removed, with photographic documentation and concurrent graft survival scoring. The scoring system utilized a 0-5 scale based on graft necrosis area [27]: 5 (necrosis < 20%), 4 (20%-40%), 3 (40%-60%), 2 (60%-80%), 1 (> 80%), and 0 (allograft removed/rejection).

On day 10 post operation (POD10), skin allografts were harvested for histopathological analysis, while spleens and graft draining lymph nodes (gdLNs) were processed into single-cell suspensions. Cells were stained with Fixable Viability Stain 575V (565694, BD Biosciences), CD45 (BV480, 752417, BD Biosciences), CD3e (BV650, 564378, BD Biosciences), CD4 (RB780, 568695, BD Biosciences), CD8a (R718, 566985, BD Biosciences), CD11b (FITC, 557396, BD Biosciences), CD11c (RB705, 756864, BD Biosciences), CD206 (AF647, 568809, BD Biosciences), CD80 (BV750, 747436, BD Biosciences), CD86 (BV421, 740034, BD Biosciences), F4/80 (PE, 111604, BioLegend), and Ly6G (APC-Cy7, 560600, BD Biosciences) for flow cytometric analysis.

To evaluate PAM pathway activity in T cells, additional flow cytometric analysis was

performed on splenic and gdLN single-cell suspensions collected on POD10. Cells were stained with Zombie NIR™ Fixable Viability Kit (423106, BioLegend), CD45 (BV480), CD3e (BV650), CD4 (APC, 100516, BioLegend), and CD8a (PE-Cy7, 552877, BD Biosciences) antibodies for surface marker identification. Subsequently, cells were fixed and permeabilized using the Cyto-Fast™ Fix/Perm Buffer Set (426803, BioLegend) according to the manufacturer's instructions, followed by intracellular staining with Phospho-Akt1 (Ser473, FITC, 11-9715-42, Invitrogen) and Phospho-4EBP1 (Thr36, Thr45, PE, 12-9107-42, Invitrogen) antibodies. Following identification of viable $CD4^+$ and $CD8a^+$ T-cell populations, p-Akt1 and p-4EBP1 expression was quantified based on mean fluorescence intensity (MFI) by flow cytometry.

2.15. Quantification of glutathione levels

To assess tissue glutathione (GSH) levels, orthotopic liver tumor and allogeneic skin transplantation models were established as described above. On day 10 after orthotopic HCC modeling, tumor tissues and adjacent non-tumor liver tissues were collected, weighed, and homogenized. For the skin transplantation model, spleen and gdLNs were harvested from recipient mice on POD 8, while spleen and axillary lymph nodes from naive C57BL/6 mice served as normal controls. All tissue homogenates were then processed using a glutathione detection kit (BC1175, Solarbio) following the manufacturer's instructions to determine GSH concentrations.

2.16. Multiplex Cytokine Profiling

On POD10, skin allografts from the aforementioned drug-treated groups were collected, minced, and homogenized, followed by centrifugation to obtain supernatants. Protein concentrations in the supernatants were quantified using the bicinchoninic acid assay (BRK0011, ABclonal), and all samples were adjusted to a final concentration of 5 mg/mL. Cytokine levels in the tissue lysates were quantified using the ABplex Mouse 9-Plex Custom Panel (RK04383, ABclonal), after which the cytokine data underwent Z-score normalization. Additionally, principal component analysis (PCA) was performed for dimensionality reduction, and the results were visualized as a two-dimensional scatter plot.

2.17. *In vivo* effect of nano-liposome in a cancer-transplant mouse model

To establish the cancer-transplant mouse model, C57BL/6 mice received subcutaneous

inoculation of 1.5 × 10^6 Hepatoma-22 cells alongside skin transplantation as described. Post-modeling, mice were randomly allocated to four treatment groups: Control (untreated), Rapa (2 mg/kg, i.p.), PF (2 mg/kg, i.p.), and PMIProsome (2 mg/kg PF-equivalent, i.v.). Allograft status was monitored daily until rejection, and tumor dimensions were measured daily throughout the study. Tumor volume (V) was calculated using the formula: V= L×W× W /2, where L (length) was greater than W (width).

2.18. Transcriptome Sequencing

RNA transcriptome profiling was executed in both parental Huh7 (Huh7-N) cells and their derived Rapa-insensitive sublines (Huh7-R) strictly adhering to the vendor's protocol. Differential gene expression was defined by stringent statistical and magnitude thresholds: significance at $p < 0.05$ combined with $\log_2$ (fold change) exceeding 1.

2.19. Histological analysis and immunostaining

Tissues were fixed in 4% paraformaldehyde for 1 week, followed by paraffin embedding. Serial sections were processed for hematoxylin and eosin (H&E) staining, immunofluorescence (IF), and immunohistochemistry (IHC). IF utilized TUNEL staining (40306ES, Yeasen) to assess apoptosis. IHC employed validated antibodies: CD3 (ab16669, Abcam) for T-cell infiltration, CD31 (ab182981, Abcam) for vascular density, and Ki67 (ab16667, Abcam) for proliferation index.

2.20. Statistical analysis

Data are presented as mean ± standard deviation (SD). Statistical analyses were performed using GraphPad Prism 9. For pairwise comparisons, unpaired two-tailed Student's t-test was employed. For group comparisons, one-way ANOVA coupled with Tukey's multiple comparisons test was applied. Statistical significance was defined as $p < 0.05$.

3. Result

3.1. Dual PI3K/mTOR Inhibitor PF-04691502 Effectively Reverses Resistance to mTOR Inhibitors in HCC

Accumulating evidence has demonstrated that feedback activation of the PI3K/Akt signaling pathway is a major mechanism underlying resistance to mTOR inhibitors [28, 29]. To

investigate the molecular basis of rapamycin (Rapa) resistance, a previously reported Rapa-resistant Huh7 cell line (Huh7-R) [27] was evaluated by transcriptomic analysis. Principal component analysis (PCA) confirmed a clear transcriptional distinction between parental Huh7 cells (Huh7-N) and Huh7-R cells (**Fig. S1**). Differential expression analysis identified extensive transcriptional alterations between Huh7-N and Huh7-R cells, as illustrated by the volcano plot **(Fig. 2A)**. Gene set enrichment analysis (GSEA) further demonstrated significant activation of the PI3K/Akt signaling pathway in Huh7-R cells relative to Huh7-N cells (**Fig. 2B** and **S2**), indicating that PI3K/Akt pathway reactivation is closely associated with acquired resistance to mTOR inhibition. To validate these findings, key signaling molecules involved in the PI3K/Akt/mTOR (PAM) pathway were examined by western blotting. Compared with Huh7-N cells, Huh7-R cells exhibited markedly increased phosphorylation levels of Akt^{Ser473}, $mTOR^{Ser2448}$, and $P70S6K^{Thr389}$ (**Fig. 2C**), consistent with activation of compensatory survival signaling. In parallel, quantitative PCR analysis demonstrated upregulated expression of multiple PAM pathway activation-associated genes in resistant cells (**Fig. 2D**), further supporting pathway hyperactivation during Rapa resistance.

Given the critical role of PI3K/Akt feedback activation in resistance development, a panel of dual PI3K/mTOR inhibitors (PMIs) was subsequently evaluated for their ability to suppress pathway signaling and overcome resistance. Western blot analysis showed that several dual inhibitors effectively inhibited phosphorylation of Akt^{Ser473} and downstream mTOR signaling molecules in Huh7-R cells, whereas Rapa induced incomplete pathway suppression and compensatory Akt activation (**Fig. 2E**). Functional screening using CCK-8 assays demonstrated that dual PI3K/mTOR inhibitors exhibited substantially enhanced cytotoxicity against both parental and resistant Huh7 cells compared with Rapa treatment (**Fig. 2F** and **S3**). Among the tested compounds, PF-04691502 (PF) displayed the most potent inhibitory activity against resistant cells while maintaining strong antitumor efficacy in parental cells. Consistently, flow cytometric analysis revealed that PF markedly induced apoptosis in both Huh7-N (**Fig. 2G-H**) and Huh7-R cells (**Fig. S4**) compared with Rapa and other inhibitors. Given the well-established role of PAM signaling in immune regulation

and its clinical relevance in preventing acute rejection after organ transplantation [27, 30], we further evaluated the immunosuppressive activities of the selected PMIs *in vitro*. Notably, PF effectively suppressed T-cell activation, as evidenced by reduced expression of IFN-γ, Granzyme B, and Perforin in $CD8^+$ T cells (**Fig. 2I-K**), while also decreasing IFN-γ production in $CD4^+$ T cells (**Fig. S5**). These findings suggest that PF not only attenuates cytotoxic T-cell effector function but also suppresses pro-inflammatory T-cell responses, thereby highlighting its potential to simultaneously exert antitumor activity and allograft-protective immunomodulatory effects.

To further assess the translational potential of dual PI3K/mTOR inhibition in the context of cancer transplantation, an *in vivo* cancer-transplant model was established to simultaneously assess antitumor efficacy and immunoregulatory activity (**Fig. S6A**). Comparative analysis of representative PMIs demonstrated that PF, Dactolisib (Dac), and VS-5584 (VS) all exhibited allograft-protective effects, as evidenced by attenuation of acute rejection manifestations, including skin crusting and allograft contraction (**Fig. S6B**-**E**). Meanwhile, PF and Dac significantly suppressed tumor progression compared with the control group (**Fig. S6F**-**H**). Although PF did not demonstrate superior overall therapeutic efficacy to Rapa, it exhibited a more favorable balance between antitumor activity and immunosuppressive efficacy among the tested PMIs (**Fig. S6**). Collectively, these *in vitro* and *in vivo* findings identify PF as the optimal PMI for simultaneously overcoming mTOR inhibitor resistance while exerting both potent antitumor and immunosuppressive effects in post-transplant HCC.

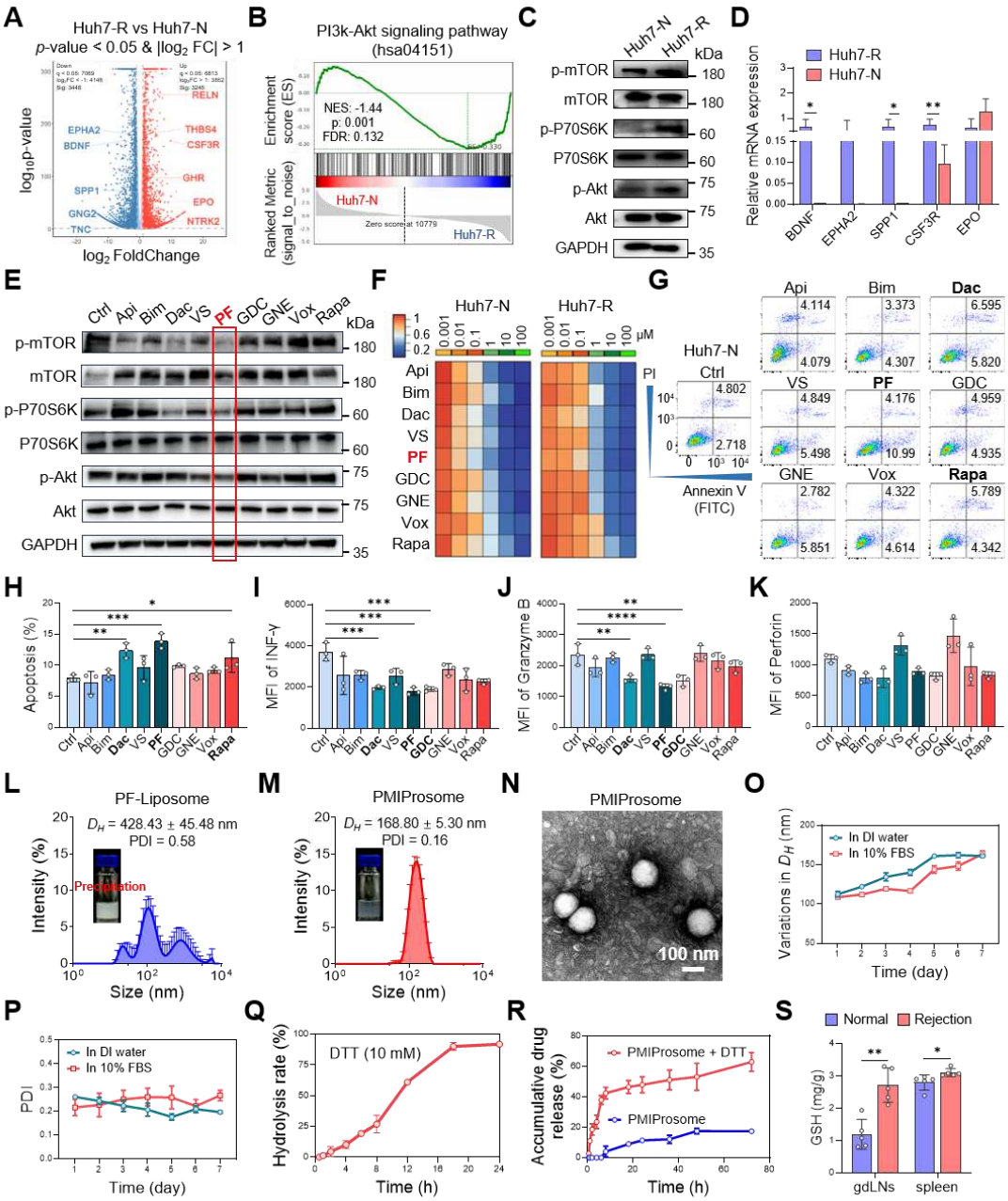


Fig.2. Rational design, characterization, and biological evaluation of PMIProsome. (A) Volcano plot of differentially expressed genes identified by transcriptomic sequencing between parental Huh7 (Huh7-N) cells and Rapa-resistant Huh7 (Huh7-R) cells. (B) Gene set enrichment analysis showing activation of the PI3K/Akt signaling pathway in Huh7-R cells compared with Huh7-N cells. (C) Western blot analysis of key PI3K/Akt/mTOR signaling pathway proteins in Huh7-N and Huh7-R cells. (D) Relative mRNA expression levels of representative PI3K/Akt/mTOR pathway-related genes in Huh7-N and Huh7-R cells. (E) Western blot analysis of key PI3K/Akt/mTOR signaling molecules in Huh7-R cells

following treatment with a panel of PI3K/mTOR inhibitors (PMIs). Control: Ctrl; Apitolisib: Api; Bimiralisib: Bim; Dactolisib: Dac; VS-5584: VS; PF-04691502: PF; GDC0084: GDC; GNE-477: GNE; Voxtalisib: Vox; Rapamycin: Rapa. (F) CCK-8 analysis of cell viability in Huh7-N and Huh7-R cells treated with different PMIs. (G) Representative flow cytometric analysis of apoptosis in Huh7-N cells following treatment with PMIs. (H) Quantitative analysis of apoptotic cell populations. (I) Quantification of IFN-γ mean fluorescence intensity (MFI) in $CD8^+$ T cells. (J) Quantification of Granzyme B MFI in $CD8^+$ T cells. (K) Quantification of Perforin MFI in $CD8^+$ T cells. (L) Particle size distribution and representative appearance of liposomes loaded with free PF, showing evident precipitation in aqueous solution. (M) Particle size distribution and representative appearance of PF prodrug-loaded liposomes (PMIProsome), exhibiting a homogeneous and transparent nanosuspension. (N) Representative transmission electron microscopy image of PMIProsome. Scale bar = 100 nm. (O) Particle size of PMIProsome in water and 10% fetal bovine serum (FBS) over 7 days. (P) Polydispersity index (PDI) of PMIProsome in water and 10% FBS over 7 days. (Q) Hydrolysis kinetics of the PF prodrug in the presence of DTT (10 mM). (R) *In vitro* drug release profiles of PMIProsome in the presence or absence of DTT (10 mM). (S) Measurement of glutathione levels in tissues. Data are presented as mean ± SD (n = 3). The statistical difference was determined by unpaired Student's t-test (D and S) and one-way ANOVA with Tukey's post hoc test (H to K): $*p < 0.05$; $**p < 0.01$; $***p < 0.001$; and $****p < 0.0001$.

3.2. Rational Design and Construction of PF-04691502 Prodrug Nanoliposome

Despite the potent dual antitumor and immunosuppressive activities of PF, its therapeutic development has been limited by poor aqueous solubility, limited formulation stability, rapid systemic clearance, and potential off-target toxicity resulting from nonspecific drug exposure. Moreover, efficient therapeutic intervention in post-transplant HCC requires synchronized drug delivery to both tumor tissues and allograft-associated inflammatory microenvironments while minimizing systemic adverse effects. To address these challenges, PF was chemically modified into a hydrophobic prodrug through conjugation with a disulfide bond-containing self-immolative linker and cholesterol moiety (**Fig. S7-9**),

followed by supramolecular assembly into PEGylated nanoliposomes (**Fig. 1A**). Compared with liposomes directly loaded with free PF, which exhibited obvious precipitation and poor colloidal stability in aqueous solution (**Fig. 2L**), PF prodrug-loaded liposomes (PMIProsome) formed a homogeneous and transparent nanosuspension with improved colloidal stability and drug compatibility (**Fig. 2M**). Dynamic light scattering analysis confirmed that PMIProsome possessed a narrow particle size distribution and favorable physicochemical characteristics suitable for systemic administration (**Fig. 2M**). Transmission electron microscopy further demonstrated that PMIProsome exhibited a uniform spherical morphology with well-defined nanostructures (**Fig. 2N**). Furthermore, the colloidal stability of PMIProsome was systematically evaluated under physiological conditions. Continuous monitoring over 7 days demonstrated that PMIProsome maintained stable particle size (**Fig. 2O**), low polydispersity index (PDI, **Fig. 2P**), and consistent zeta potential (**Fig. S10**) in both water and fetal bovine serum (FBS), without evident aggregation or structural instability.

To investigate the redox-responsiveness of the prodrug design, the cleavage behavior of the PF prodrug was evaluated under reducing conditions. HPLC analysis demonstrated that the disulfide-containing prodrug underwent rapid hydrolysis in the presence of DTT, leading to efficient regeneration of active PF (**Fig. 2Q**). Consistently, PMIProsome displayed markedly accelerated drug release under reducing conditions, whereas only minimal drug leakage was observed in PBS without DTT stimulation (**Fig. 2R**), indicating that the nanoplatform enables reduction-triggered and site-responsive drug release. Importantly, glutathione (GSH) analysis revealed significantly elevated GSH levels in the spleens and graft-draining lymph nodes (gdLNs) from mice undergoing acute allogeneic graft rejection compared with normal tissues (**Fig. 2S**), while orthotopic liver tumors also exhibited markedly higher GSH levels than adjacent non-tumor liver tissues (**Fig. S11**). These findings suggest that both tumor tissues and allograft rejection-associated immune microenvironments possess enhanced reductive characteristics, thereby supporting preferential PF release under reductive conditions within pathological microenvironments.

3.3. PF-04691502-Mediated PI3K/mTOR Blockade Provides the Pharmacological Basis for Sustained HCC Suppression

Following the successful construction of the redox-responsive PMIProsome, we next investigated whether PF and its nanoliposomal formulation retained potent antitumor activity against HCC cells *in vitro*. Comparative analyses were performed using four HCC cell lines, including HCCLM3, SNU-449, Hepa1-6, and Hepatoma-22 cells, to evaluate the therapeutic efficacy of PF, Rapa, and PMIProsome. Consistent with the enhanced pathway inhibition observed in resistant HCC cells, PF exhibited substantially stronger antiproliferative activity than Rapa across multiple HCC cell lines. CCK-8 assays demonstrated that PF more effectively suppressed tumor cell viability, whereas PMIProsome retained considerable inhibitory activity despite showing moderately reduced potency compared with free PF (**Fig. 3A**). Similar trends were observed in colony formation assays, in which PF markedly impaired long-term clonogenic growth relative to Rapa (**Fig. 3B**-**C**). Furthermore, EdU incorporation analysis revealed that PF treatment markedly reduced the proportion of proliferating tumor cells compared with the Rapa-treated group (**Fig. 3D**-**E**). The superior antitumor efficacy of PF was further supported by flow cytometric analyses of apoptosis and cell-cycle progression. PF treatment induced substantially higher levels of tumor cell apoptosis than Rapa and PMIProsome across the tested HCC cell lines (**Fig. 3F**-**G** and **S12**). In parallel, PF more effectively arrested tumor cells at the G0/G1 phase, indicating potent suppression of cell-cycle progression (**Fig. 3H**-**I**).

Although PMIProsome exhibited attenuated *in vitro* efficacy relative to free PF, they retained substantial antitumor activity comparable to that of Rapa (**Fig. 3A**-**I**). This reduction in immediate cytotoxic potency may be attributable to the sustained-release characteristics of the nanoliposomal formulation, which could delay liberation of active PF. In addition, cellular uptake kinetics and the requirement for reductive microenvironment-dependent prodrug activation may further contribute to the delayed pharmacodynamic response of PMIProsome under conventional *in vitro* culture conditions. To further investigate the mechanism underlying the enhanced antitumor activity of PF, we evaluated its effects on PAM signaling. PF treatment markedly reduced the mRNA expression of PAM

pathway-associated genes, including *EPHA2*, *CSF3R*, and *EPO*, compared with Rapa treatment (**Fig. S13**). Consistently, PF also induced stronger suppression of $mTOR^{Ser2448}$, Akt^{Ser473}, $P70S6K^{Thr389}$, and $4EBP1^{Thr37/46}$ phosphorylation, indicating more complete blockade of PAM signaling than conventional mTOR inhibition (**Fig. 3J**). These results demonstrate that PF exerts superior antitumor activity compared with Rapa through more effective inhibition of PAM signaling, while PMIProsome successfully preserve the therapeutic activity of PF and provide a functional nanoplatform for sustained and responsive drug delivery.

3.4. PF-04691502 Demonstrates Potent Immunosuppressive Activity *in vitro*

In addition to its central role in tumor progression and therapeutic resistance, the PAM signaling pathway is also critically involved in immune activation and effector differentiation of immune cells during allograft rejection [31]. Given the potent inhibitory effects of PF on PAM signaling in HCC cells, we next investigated whether PF and PMIProsome could simultaneously modulate immune cell activation *in vitro*. PF maintained immunosuppressive activity comparable to Rapa in restraining T-cell proliferation, as evidenced by marked inhibition of both $CD4^+$ and $CD8^+$ T-cell expansion in CFSE dilution assays (**Fig. 3K-L**). PMIProsome showed slightly reduced suppression of T-cell proliferation, likely due to the sustained-release properties of the nanoliposomal formulation. Consistent with T-cell suppression, PF treatment markedly downregulated the expression of PAM pathway-associated genes in activated immune cells, indicating effective inhibition of immune activation-related signaling (**Fig. S14**).

Considering the pivotal role of dendritic cells (DCs) in initiating alloimmune responses through antigen presentation and costimulatory signaling [32], we next evaluated the effects of PF on DC maturation. PF more effectively suppressed DC activation and maturation than Rapa, as evidenced by reduced expression of antigen presentation and costimulatory markers, including CD80, CD86 (**Fig. 3M-N**), and MHC-II (**Fig. S15**). Moreover, the decreased proportion of $H\text{-}2K^b$ SIINFEKL-positive cells further suggested impaired antigen presentation capacity following PF treatment (**Fig. 3M-N**). Notably, PMIProsome reshaped the cytokine profile of DCs by suppressing the expression of pro-inflammatory cytokines

(IL-6, IL-1β, and IFN-γ) while enhancing IL-10 expression, indicating a transition toward a more tolerogenic immune phenotype [33] (**Fig. 3O**). Together, these results establish PF as a potent dual-function agent capable of inhibiting tumor-associated PAM signaling while restraining cellular processes underlying alloimmune activation.

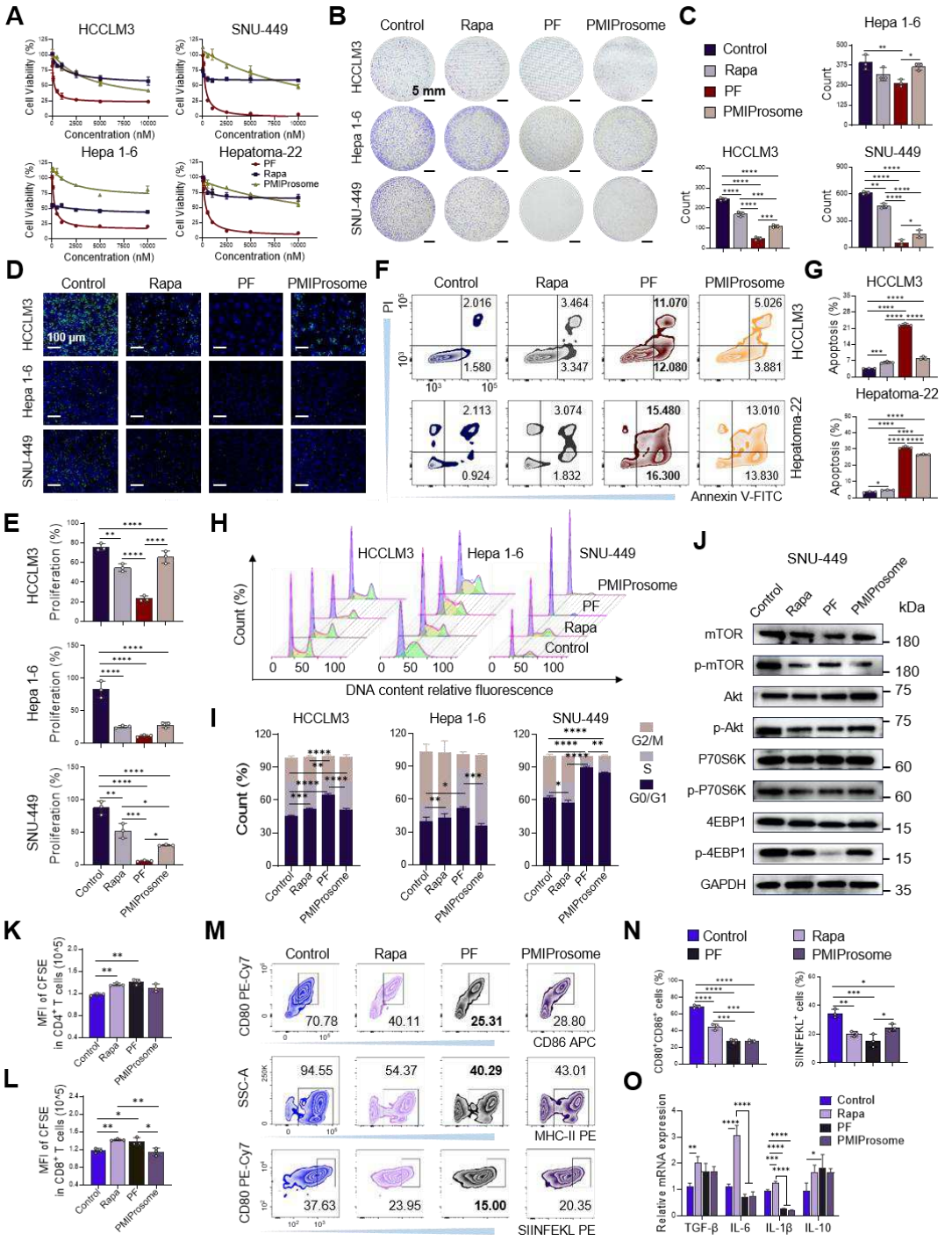


Fig.3. *In vitro* analysis of PMIProsome-mediated regulation of tumor cells and immune cells. (A) CCK-8 assay for cell viability. (B) Representative images of colony

formation. Scale bar = 5 mm. (C) Quantification of colony formation efficiency. Colony numbers were counted using ImageJ. (D) Representative images of the EdU proliferation assay. Green: EdU-positive cells; blue: DAPI-stained nuclei. Scale bar = 100 μm. (E) Quantification of EdU-positive cell percentage. (F) Representative dot plots show early and late apoptotic populations. (G) Quantification of total apoptosis (early and late). (H) Representative histograms show DNA content distribution (G0/G1, S, G2/M phases). (I) Quantification of cell cycle phase distribution. (J) Western blot analysis of protein expression levels of key components in the PI3K/mTOR signaling pathway. (K) Mean fluorescence intensity of CFSE in $CD4^+$ T cells. (L) Mean fluorescence intensity of CFSE in $CD8^+$ T cells. (M) Representative pseudocolor flow cytometry plots showing BMDC maturation markers (CD80 and CD86), $OVA_{257-264}$ peptide presentation (H-$2K^b$-SIINFEKL complex), and MHC-II expression. (N) Quantification of $CD80^+CD86^+$ BMDCs and H-$2K^b$-$SIINFEKL^+$ BMDCs. (O) qPCR analysis of gene expression in BMDCs. Data are presented as mean ± SD (n = 3). The statistical difference was determined by one-way ANOVA with Tukey's post hoc test: *$p < 0.05$; **$p < 0.01$; ***$p < 0.001$; and ****$p < 0.0001$.

3.5. PMIProsome Improves Tumor Exposure and Sustains PF Delivery In Vivo

Given the potent antitumor and immunomodulatory activities of PF together with the favorable physicochemical properties of PMIProsome, we next investigated whether nanoliposomal delivery could improve *in vivo* drug accumulation within tumor tissues. Compared with free small-molecule drugs, nanoliposomes with appropriate particle size generally exhibit prolonged blood circulation and enhanced tumor retention [23], while the elevated reductive microenvironment in tumors may further facilitate GSH-responsive drug release from PMIProsome (**Fig. S11**). To evaluate the *in vivo* transport and biodistribution profiles, the near-infrared fluorescent probe DiR was encapsulated into PMIProsome or co-formulated with free PF, followed by longitudinal IVIS imaging in Hepatoma-22 tumor-bearing mice after systemic administration (**Fig. 4A**). Whole-body fluorescence imaging revealed substantially enhanced tumor accumulation in the PMIProsome group compared with free drug treatment throughout the 5-day observation period (**Fig. 4B**). In particular, PMIProsome maintained persistent fluorescence signals within tumor tissues at later time

points, whereas fluorescence intensity in the free drug group gradually diminished over time, suggesting improved intratumoral retention mediated by nanoliposomal delivery. *Ex vivo* imaging of harvested tissues further confirmed markedly stronger fluorescence signals in tumors from PMIProsome-treated mice (**Fig. 4C**-**E** and **S16**-**18**). To further quantitatively assess intratumoral drug delivery, PF concentrations in tumor tissues were directly measured by HPLC at 12 and 48 h after administration. Consistent with the fluorescence imaging results, PMIProsome achieved significantly higher intratumoral drug accumulation than free PF treatment at both time points (**Fig. 4F**), indicating improved tumor delivery efficiency and retention capacity. Overall, these findings confirm that PMIProsome overcome the limited tumor accumulation of free PF and provide a delivery strategy for sustained intratumoral drug exposure in HCC.

3.6. PMIProsome Improves the Therapeutic Biosafety Profile of PF *in vivo*

Although enhanced tumor accumulation is essential for maximizing therapeutic efficacy, systemic administration of PMIs inevitably raises concerns regarding off-target toxicity and dose-limiting adverse effects [34]. Therefore, we next investigated whether nano-liposomal encapsulation could improve systemic tolerability while maintaining favorable safety profiles *in vivo*. Healthy C57BL/6 mice were administered free PF or PMIProsome at escalating doses, followed by comprehensive assessments of body weight, hematological parameters, serum biochemical indices, and histopathological changes (**Fig. 4G**). Throughout the treatment period, no obvious alterations in body weight were observed in either free PF- or PMIProsome-treated mice, indicating that repeated administration was generally well tolerated (**Fig. 4H**). Comprehensive hematological analyses further demonstrated that PMIProsome treatment did not induce significant alterations in white blood cells, lymphocytes, neutrophils, red blood cells, platelet counts, or hemoglobin levels compared with untreated controls (**Fig. 4I**-**J** and **S19**), suggesting minimal hematopoietic toxicity following systemic administration. Notably, mice receiving free PF exhibited a mild but non-significant reduction in total white blood cell counts, which was primarily attributable to decreased lymphocyte numbers. This trend is consistent with the established T-cell suppressive activity of mTOR inhibition [9, 27] and did not indicate overt

myelosuppression (**Fig. 4I-J**).

Serum biochemical analyses revealed that aspartate aminotransferase (AST, **Fig. 4K**) and blood urea nitrogen (BUN, **Fig. 4L**) levels remained largely unchanged among the different groups. Notably, dose escalation of free PF resulted in moderate increases in alanine aminotransferase (ALT, **Fig. 4M**) and creatinine levels (CR, **Fig. 4N**), indicating the onset of hepatic and renal dysfunction. In contrast, mice treated with equivalent doses of PMIProsome exhibited markedly attenuated changes in these parameters, suggesting that nano-liposomal encapsulation effectively mitigated PF-associated systemic toxicity (**Fig. 4M-N**). Histopathological examination of major organs, including the heart, liver, spleen, lung, and kidney, further confirmed the favorable biosafety profile of PMIProsome (**Fig. 4O**). No obvious tissue injury, inflammatory infiltration, or structural abnormalities were observed, even after administration at the highest tested dose. To further evaluate long-term safety, additional mice receiving high-dose free PF or PMIProsome were monitored for 30 days after treatment. Hematological and biochemical analyses performed at the end of the observation period revealed no significant abnormalities in either group, indicating the absence of delayed systemic toxicity and supporting the favorable long-term tolerability of PMIProsome (**Fig. S20**). PMIProsome exhibited excellent *in vivo* biocompatibility and substantially reduced PF-associated systemic toxicity, supporting their further evaluation for antitumor and immunomodulatory applications.

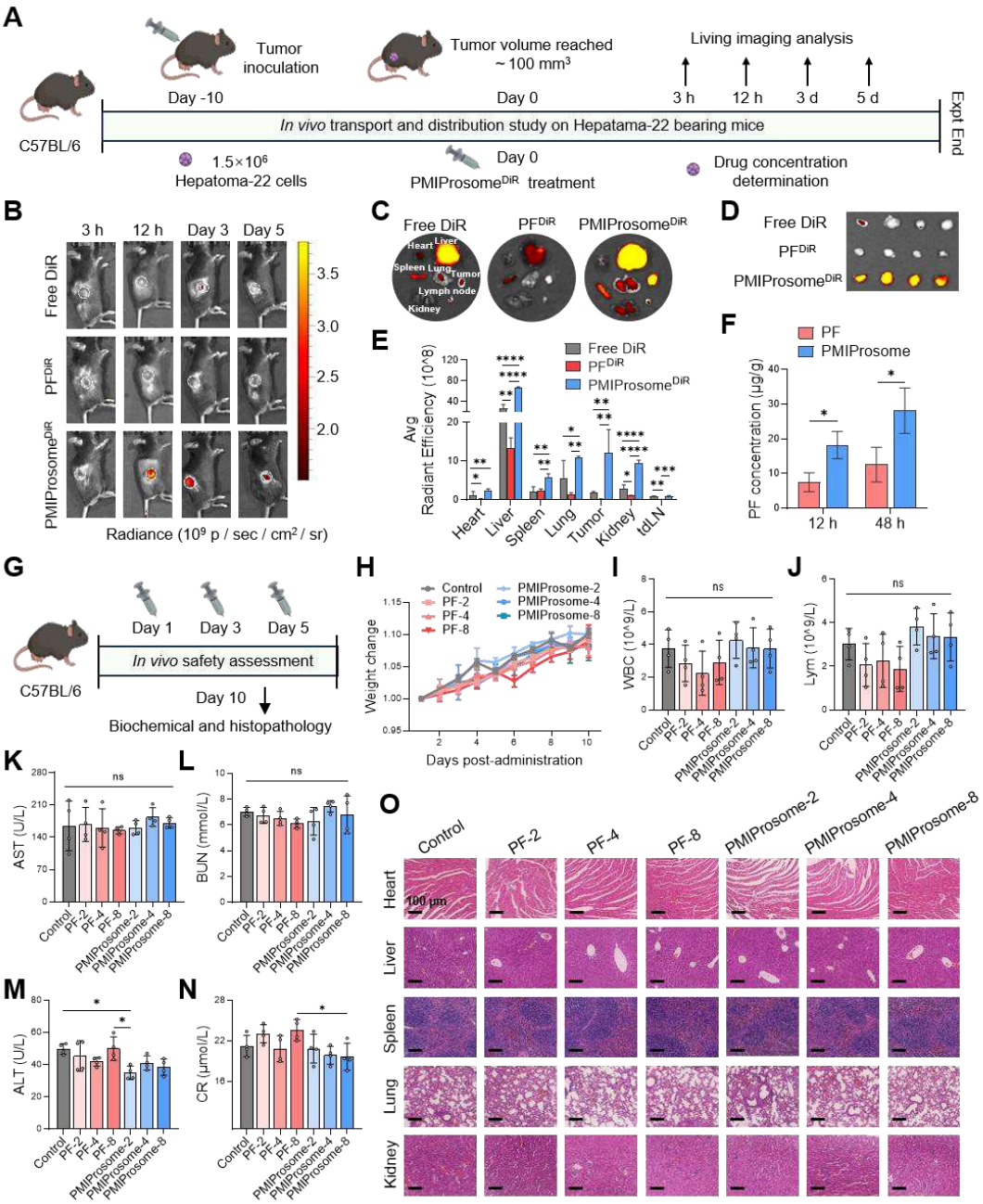


Fig.4. PMIProsome exhibits prolonged tumor retention and favorable systemic biosafety *in vivo*. (A) Schematic illustration of the experimental design for *in vivo* biodistribution analysis in Hepatoma-22-bearing mice. (B) Representative whole-body fluorescence images acquired at 3 h, 12 h, Day 3, and Day 5 following administration. (C) Representative *ex vivo* fluorescence images of major organs (heart, liver, spleen, lung, tumor, kidney, and lymph node) collected 12 h after injection. (D) Representative *ex vivo* fluorescence images of tumors harvested 12 h after administration. (E) Quantitative analysis of fluorescence intensity in major organs and tumors based on *ex vivo* imaging.

(F) Quantification of intratumoral PF concentrations at the indicated time points by HPLC. (G) Schematic illustration of the experimental protocol for *in vivo* safety evaluation. (H) Changes in body weight during treatment. (I-J) Peripheral blood white blood cell and lymphocyte counts following repeated administration. (K-N) Serum biochemical analyses of aspartate aminotransferase (AST), blood urea nitrogen (BUN), alanine aminotransferase (ALT), and creatinine (CR). (O) Representative H&E-stained sections of major organs, including the heart, liver, spleen, lung, and kidney, collected from mice treated with free PF or PMIProsome. Scare bar = 100 μm. Data are presented as mean ± SD (n = 4). The statistical difference judged was determined by one-way ANOVA with Tukey's post hoc test (E and H to N) and unpaired Student's t-test (F): *$p < 0.05$; **$p < 0.01$; ***$p < 0.001$; ****$p < 0.0001$; and ns, not significant.

3.7. PMIProsome Achieves Sustained Tumor Suppression in an Orthotopic Hepatocellular Carcinoma Model

Having demonstrated enhanced tumor accumulation and favorable systemic tolerability, we next investigated whether these advantages could be translated into improved therapeutic efficacy *in vivo*. To this end, an orthotopic HCC model was established using luciferase-expressing Hepa1-6 cells, and tumor progression was longitudinally monitored by bioluminescence imaging following treatment with PMIProsome, free PF, or Rapa (**Fig. 5A**). Consistent with the enhanced intratumoral drug accumulation observed previously (**Fig. 4D-F**), PMIProsome exerted markedly superior and more durable antitumor activity than either free PF or Rapa (**Fig. 5B-D**). Although both free PF and Rapa transiently delayed tumor progression, as reflected by reduced bioluminescence signals at post-administration day 8 (PAD 8), tumor growth gradually resumed thereafter. In contrast, PMIProsome-treated mice maintained substantially lower tumor burdens throughout the observation period, with significantly diminished fluorescence signals still evident at PAD 12 (**Fig. 5D**), indicating sustained tumor control following systemic delivery.

The superior tumor inhibition achieved by PMIProsome was further translated into a survival advantage. While both free PF (19.0 ± 2.8 days) and Rapa (18.5 ± 3.2 days)

moderately prolonged survival compared with saline-treated controls (12.8 ± 1.9 days), PMIProsome exhibited the most pronounced benefit (**Fig. 5E**). Notably, two of six mice receiving PMIProsome remained free of ascites during the entire 40-day observation period, suggesting durable suppression of disease progression (**Fig. 5E**). Meanwhile, no obvious body weight loss was observed in any treatment group, further supporting the favorable tolerability of PMIProsome (**Fig. 5F**). Histological analyses further corroborated the superior antitumor activity of PMIProsome. Immunohistochemical staining demonstrated significantly reduced expression of Ki67 and CD31 in PMIProsome-treated tumors, indicating effective suppression of tumor cell proliferation and angiogenesis, respectively (**Fig. 5G-I**). Consistent with these findings, TUNEL staining revealed a pronounced increase in apoptotic cells following PMIProsome treatment, further confirming the enhanced tumoricidal activity of the nanoliposomal formulation (**Fig. 5G** and **J**).

To determine whether the enhanced therapeutic efficacy of PMIProsome was associated with more effective blockade of the PAM signaling cascade *in vivo*, tumor tissues were further subjected to molecular analyses. Quantitative PCR analysis demonstrated that PMIProsome treatment significantly reduced the expression of multiple genes associated with PAM signaling (**Fig. 5K**). Consistently, western blot analysis demonstrated markedly reduced phosphorylation of key mTOR signaling components, indicating effective suppression of PAM pathway activity *in vivo* (**Fig. 5L**). By enabling sustained PF exposure in tumors, PMIProsome achieved prolonged PI3K/mTOR pathway inhibition and enhanced antitumor efficacy compared with free PF and Rapa treatment in orthotopic HCC.

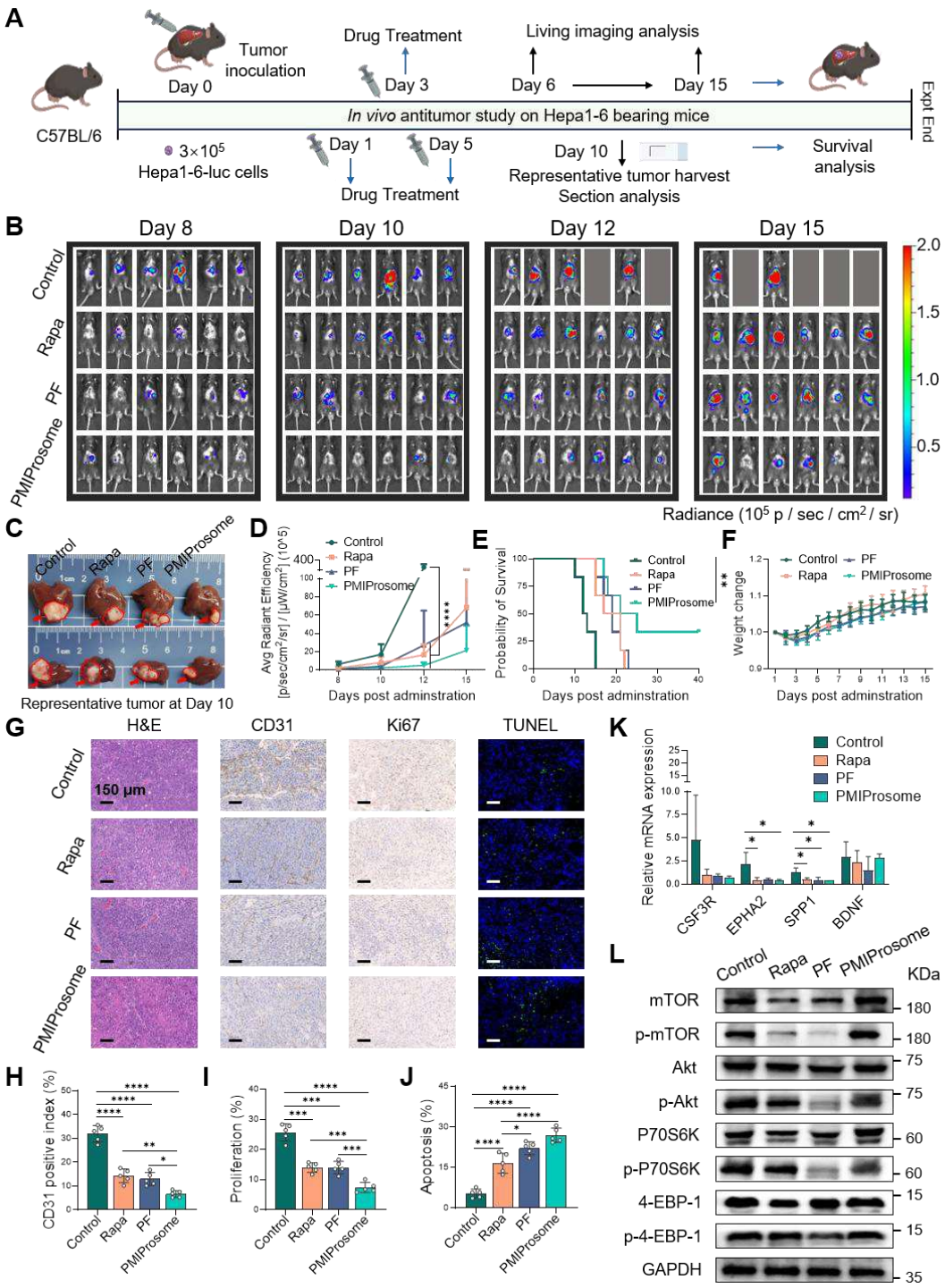


Fig.5. PMIProsome exerts potent antitumor activity in an orthotopic hepatocellular carcinoma model. (A) Schematic illustration of the experimental design for evaluating the therapeutic efficacy of PMIProsome in orthotopic Hepa1-6-luc HCC-bearing mice. (B) Representative *in vivo* bioluminescence images of orthotopic Hepa1-6-luc tumors acquired at the indicated time points following treatment. (C) Representative gross images of livers harvested from different treatment groups. Upper panels show whole livers, and lower

panels show tumor-bearing liver lobes. (D) Longitudinal quantification of tumor bioluminescence signals during treatment. (E) Kaplan-Meier survival analysis of tumor-bearing mice. Survival was monitored until the development of severe tumor burden-associated ascites. (F) Body weight profiles of mice throughout the treatment period. (G) Representative histological and immunostaining analyses of tumor tissues collected at Day 10 post-inoculation. Scare bar = 100 μm. (H-J) Quantitative analysis of CD31-positive areas, proliferating cell fractions, and apoptotic cell fractions in tumor sections, calculated using ImageJ software. (K) Relative mRNA expression levels of key PAM pathway-associated genes in tumor tissues. (L) Western blot analysis of PAM pathway-related proteins in tumor tissues following different treatments. Data are presented as mean ± SD (n = 5-6 in D to J, and n = 3 in K). Statistical significance was assessed by two-way ANOVA followed by Tukey's post hoc test (D and F), log-rank (Mantel−Cox) test (E) or one-way ANOVA with Tukey's post hoc test (H to K): *p < 0.05; **p < 0.01; ***p < 0.001; ****p < 0.0001; and ns, not significant.

3.8. PMIProsome Alleviates Allogeneic Skin Graft Rejection via Systemic and Local Immune Modulation

Given that PAM signaling regulates not only tumor cell proliferation but also T-cell activation and dendritic cell maturation, and considering the observed suppression of PI3K/mTOR activity-associated immune effector functions *in vitro*, we next hypothesized that systemic administration of PMIProsome may exert immunomodulatory effects *in vivo*. We therefore evaluated PMIProsome in a fully mismatched skin transplantation model to determine its potential in regulating allograft rejection (**Fig. 6A**). All treatment groups exhibited stable body weight throughout the observation period, indicating favorable systemic tolerability of all formulations (**Fig. 6B**). Postoperative monitoring revealed rapid progression of acute rejection in saline- and free PF-treated groups, characterized by pronounced allograft contraction, eschar formation, and necrosis beginning at POD 8 (**Fig. 6C**). In contrast, both Rapa and PMIProsome treatment markedly preserved allograft morphology, maintaining structural integrity and tight allograft-host adhesion (**Fig. 6C**). Consistent with these observations, quantitative evaluation demonstrated that PMIProsome (17.4 ± 1.7 days)

significantly improved allograft survival scores and prolonged overall allograft survival compared with saline (10.8 ± 0.9 days) and free PF groups (12.1 ± 2.0 days), achieving outcomes comparable to Rapa (15.1 ± 3.2 days) without significant differences between the two (**Fig. 6D-E**). Histological analysis of allograft tissues further substantiated these findings. H&E staining revealed that PMIProsome preserved tissue architecture with reduced inflammatory disruption and improved epidermal-dermal integrity (**Fig. 6F**). A marked reduction in $CD3^+$ T-cell infiltration indicated effective suppression of alloimmune cell recruitment within the allograft (**Fig. 6F**).

To elucidate the systemic immunological basis underlying these effects, we next analyzed peripheral immune organs (PIOs), including the spleen and graft-draining lymph nodes (gdLNs), which are central hubs for antigen presentation and T-cell priming [35]. Flow cytometric analysis revealed that PMIProsome significantly reduced the proportion of $CD8^+$ cytotoxic T cells in both compartments, accompanied by a decreased $CD8^+/CD4^+$ T-cell ratio, indicating reduced cytotoxic immune dominance (**Fig. 6G-H**). To investigate the underlying mechanisms of T cell regulation *in vivo*, we analyzed PI3K/mTOR pathway activation in recipient T cells isolated from PIOs. Flow cytometric analysis revealed that PMIProsome treatment reduced phosphorylation levels of AKT and 4EBP1 in T cells compared with saline and free PF groups, with effects comparable to Rapa (**Fig. 6I-J** and **Fig. S21**). These results indicate that PMIProsome suppresses alloimmune activation through sustained inhibition of PAM signaling in T cells. PMIProsome also modulated antigen-presenting cell activity. In gdLNs, it significantly reduced DC abundance and maturation, as evidenced by decreased $CD11c^+$ populations and CD80/CD86 expression, whereas free PF and Rapa exhibited only partial or non-significant effects (**Fig. 6K-L**). In the spleen, dendritic cell frequency was also reduced but did not reach statistical significance (**Fig. S22**). Extended immune phenotyping showed minimal effects on neutrophil populations (**Fig. S23**). In parallel, macrophage subset analysis indicated a shift toward a less inflammatory phenotype, characterized by reduced $CD11b^+F4/80^+$ macrophage populations in gdLNs (**Fig. S24**) and increased CD206 expression in gdLNs and spleen (**Fig. S24-25**). Overall, PMIProsome mediated coordinated suppression of

cytotoxic T-cell responses and antigen-presenting cell activation across peripheral immune compartments.

To further characterize immune polarization at the allograft site, multiplex cytokine profiling was performed. PMIProsome markedly suppressed multiple pro-inflammatory cytokines, including IL-2 and IL-1β, while reshaping the overall cytokine landscape toward an anti-inflammatory profile [36], as confirmed by Z-score normalization and PCA analysis (**Fig. 6M-N**). Notably, the cytokine signature of PMIProsome closely resembled that of Rapa but displayed broader suppression of inflammatory mediators (**Fig. 6M-N**). These results indicate that PMIProsome preserves allogeneic skin grafts by suppressing PAM signaling in immune cells and attenuating alloimmune activation, ultimately prolonging allograft survival.

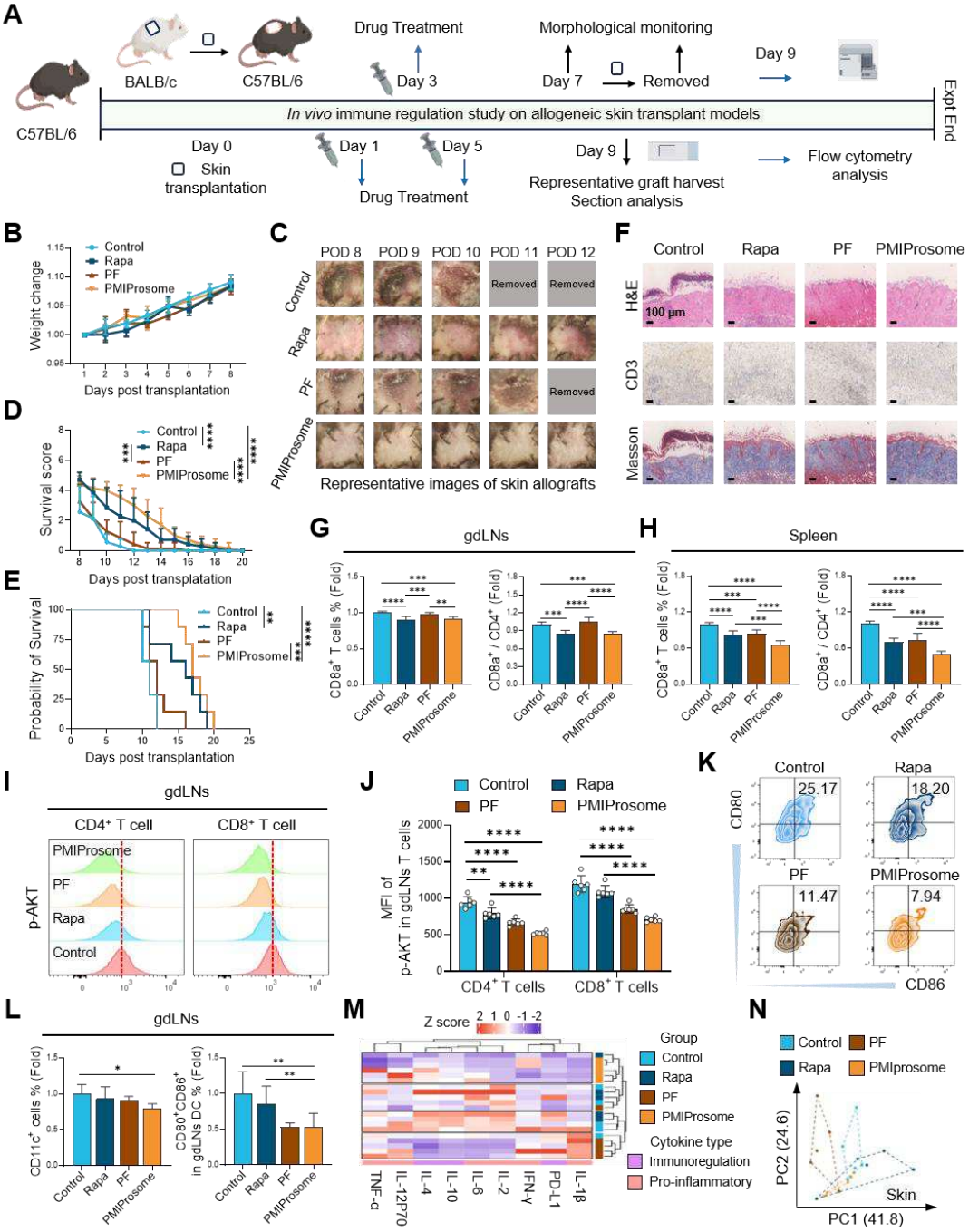


Fig.6. Immunomodulatory effects of PMIProsome in allogeneic skin transplantation. (A) Schematic illustration of the experimental design for evaluating PMIProsome in an allogeneic skin transplant model. (B) Body weight changes of mice during treatment across different groups. (C) Representative images of allogeneic skin grafts. “Removed” indicates complete allograft detachment at the corresponding time points. (D) Allograft survival scores over the observation period post-transplantation. (E) Kaplan-Meier survival analysis of allogeneic skin grafts, monitored until complete allograft rejection. (F) Histological

analysis of skin allografts at POD 9, including H&E staining, CD3 immunohistochemistry, and Masson's trichrome staining. Scale bar = 100 μm. (G) Frequencies of $CD8^+$ T cells and $CD8^+/CD4^+$ T-cell ratios in graft-draining lymph nodes (gdLNs). Values were normalized to the mean value of the Control group and were presented as fold changes. (H) Frequencies of $CD8^+$ T cells and $CD8^+/CD4^+$ ratios in spleen. Representative flow cytometry histograms (I) and quantitative analyses of p-AKT expression in $CD4^+$ and $CD8^+$ T cells (J) isolated from the graft-draining lymph nodes. (K) Representative flow cytometry plots showing CD80 and CD86 expression on dendritic cells in gdLNs. (L) Quantification of $CD11c^+$ dendritic cells and $CD80^+CD86^+$ double-positive mature dendritic cells in gdLNs. (M) Heatmap of pro-inflammatory and immunoregulatory cytokines in allograft tissues, displayed as Z-score-normalized expression values. (N) Principal component analysis of cytokine profiles in skin allograft tissues from different treatment groups. Data are presented as mean ± SD (n = 6-7 in B to L, and n = 5 in M and N). Statistical significance was assessed by two-way ANOVA followed by Tukey's post hoc test (B and D), log-rank (Mantel−Cox) test (E), or one-way ANOVA with Tukey's post hoc test (G to L): $*p < 0.05$; $**p < 0.01$; $***p < 0.001$; $****p < 0.0001$; and ns, not significant.

3.9. PMIProsome Simultaneously Suppresses Tumor Progression and Allograft Rejection in a Cancer–Transplant Concomitant Model

To evaluate whether PMIProsome could achieve a functional balance between tumor control and transplant immune protection under clinically relevant competing demands, we established a concomitant cancer-transplant model by combining subcutaneous Hepatoma-22 tumor implantation with allogeneic skin transplantation (**Fig. 7A**). This setup mimics the clinical scenario of malignancy in transplant recipients. All treatment groups exhibited stable body weight throughout the study period, indicating good systemic tolerability of both the disease model and interventions (**Fig. 7B**). In the transplantation compartment, PMIProsome and Rapa significantly delayed the onset of rejection-associated phenotypes, including allograft contraction and necrosis (**Fig. 7C**), and markedly improved allograft survival scores (**Fig. 7D**). Consistently, survival analysis demonstrated prolonged allograft survival in both Rapa (16.9 ± 2.1 days) and PMIProsome

(18.7 ± 2.5 days) groups compared with free drug (14.6 ± 1.1 days) and control (11.7 ± 1.5 days) cohorts (**Fig. 7E**), with PMIProsome showing the most durable protection.

Importantly, in parallel with effective allograft protection, PMIProsome also exerted superior tumor growth inhibition compared with all other treatment groups (**Fig. 7F**-**G**). Longitudinal tumor monitoring revealed consistently suppressed tumor progression in the PMIProsome group, whereas free drug and Rapa exhibited only partial or moderate tumor control (**Fig. 7F**-**G**). *Ex vivo* tumor analysis further confirmed reduced tumor burden and enhanced therapeutic response in PMIProsome-treated mice (**Fig. 7H**). Histopathological evaluation substantiated these dual effects. In the allografts, PMIProsome preserved epidermal integrity and collagen architecture while reducing T-cell infiltration (**Fig. 7I**). In tumor tissues, PMIProsome induced pronounced tumor cell apoptosis and reduced proliferative activity, indicating robust antitumor efficacy (**Fig. 7I**). These results demonstrate that PMIProsome provides a dual-functional therapeutic strategy by coordinating tumor suppression with alloimmune regulation in a clinically relevant cancer-transplant setting.

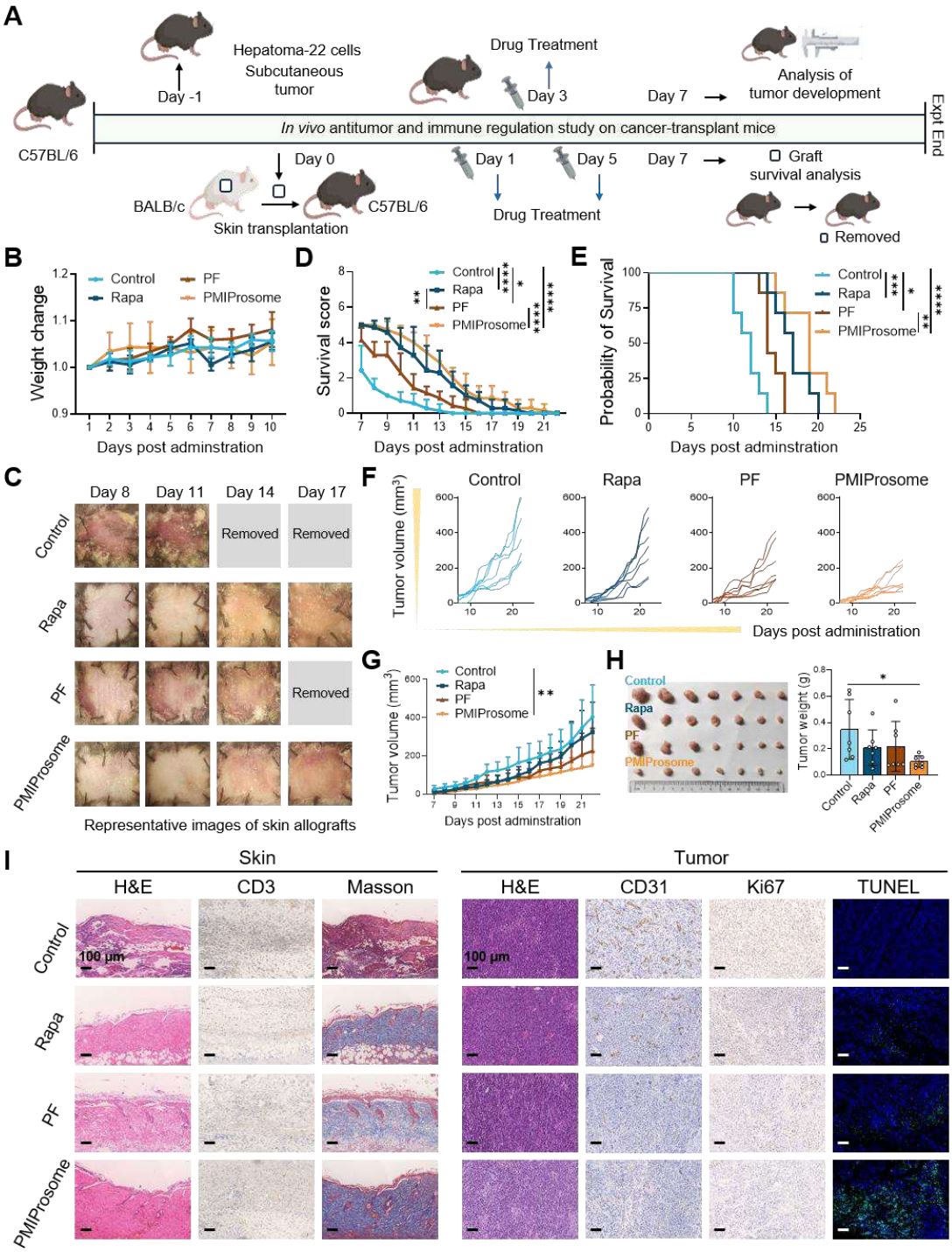


Fig.7. PMIProsome coordinates tumor suppression and allograft protection in a cancer-transplant model. (A) Schematic illustration of the experimental design integrating subcutaneous Hepatoma-22 tumor implantation with allogeneic skin transplantation to evaluate dual antitumor and immunoregulatory efficacy of PMIProsome. (B) Body weight changes of mice across different treatment groups during the study period. (C) Representative images of allogeneic skin grafts. “Removed” indicates complete

allograft rejection at the corresponding time points. (D) Allograft survival scores over time following transplantation. (E) Kaplan-Meier analysis of allogeneic skin graft survival in different treatment groups. (F) Individual tumor growth curves of subcutaneous Hepatoma-22 tumors in each mouse. (G) Quantification of tumor volume changes over the observation period. (H) Representative images and corresponding weights of harvested subcutaneous tumors at endpoint. (I) Histopathological analysis of skin allografts and tumor tissues, including H&E staining, immunohistochemistry, and Masson's trichrome staining. Scare bar = 100 μm. Data are presented as mean ± SD (n = 7). Statistical significance was assessed by two-way ANOVA followed by Tukey's post hoc test (B, D, and G), log-rank (Mantel−Cox) test (E), or one-way ANOVA with Tukey's post hoc test (H): *$p < 0.05$; **$p < 0.01$; ***$p < 0.001$; ****$p < 0.0001$; and ns, not significant.

4. Discussion

Liver transplantation remains the most effective curative treatment for selected patients with HCC [37]. However, long-term outcomes continue to be compromised by the need to simultaneously maintain durable immunosuppression for allograft protection and effective antitumor activity to prevent tumor recurrence [38, 39]. Although advances in surgical techniques and perioperative management have substantially improved early allograft survival [40], tumor recurrence after transplantation remains a leading cause of late mortality [41, 42]. Current pharmacological strategies have only partially addressed this clinical challenge. Calcineurin inhibitor-based immunosuppressive regimens effectively control alloimmune responses but are associated with an increased risk of tumor progression [43]. In contrast, mTOR inhibitors provide both immunosuppressive and antitumor activities [7, 44], yet their clinical benefits are often limited by compensatory activation of the PAM signaling network, unfavorable pharmacokinetic properties, and dose-dependent systemic toxicity [9, 45].

In this study, we demonstrate that these limitations can be partially addressed through delivery-guided optimization of dual PI3K/mTOR inhibition rather than further increasing inhibitor potency alone. Although dual PI3K/mTOR inhibition represents an attractive

strategy for transplant-associated malignancies because of its combined antitumor and immunomodulatory activities [10, 46], its clinical potential remains incompletely realized [47, 48]. The intrinsic potency of PF may not be the primary determinant of its therapeutic performance [49]. Instead, rapid systemic distribution, insufficient retention within pathological tissues, and dose-dependent toxicity may restrict sustained pathway inhibition and ultimately narrow its therapeutic window [21]. This challenge reflects a broader limitation in targeted therapy, where increased molecular potency does not necessarily translate into improved therapeutic efficacy. Excessive systemic inhibition of essential signaling networks may result in toxicity, whereas insufficient drug exposure allows adaptive pathway recovery. Therefore, controlling the spatial and temporal characteristics of pathway inhibition represents an essential aspect of therapeutic design. Importantly, this study is conceptually distinct from our previous nanotherapy that combined SN38 with rapamycin for concurrent antitumor and immunosuppressive effects [27]. Here, a single dual PI3K/mTOR inhibitor simultaneously targets oncogenic signaling and alloimmune activation, shifting the therapeutic paradigm from drug combination to pathway-based coordination of tumor control and allograft protection.

The prodrug strategy employed in PMIProsome helped overcome these limitations by integrating PF into the nanoliposomal architecture through cholesterol conjugation, thereby improving compatibility with the lipid bilayer and enhancing formulation integrity. Meanwhile, incorporation of a disulfide-containing linker enabled reduction-responsive release of active PF, providing a mechanism for drug release while minimizing premature leakage during circulation. Unlike conventional nanocarrier formulations in which therapeutic molecules and delivery vehicles remain physically independent [50], prodrug engineering established a molecular connection between PF and the nanoliposomal structure, allowing the carrier to regulate not only drug stability but also activation behavior. Thus, the nanocarrier functioned not merely as a passive delivery vehicle but as a regulator of drug stability, distribution, and pharmacodynamic persistence [23].

One notable observation of this study was that the therapeutic advantage of PMIProsome

became evident primarily under *in vivo* conditions. Although free PF exhibited stronger immediate cytotoxicity in conventional cell-based assays, PMIProsome achieved superior therapeutic outcomes in orthotopic HCC, allogeneic transplantation, and combined tumor-allograft models. This apparent discrepancy reflects the distinct pharmacological requirements between *in vitro* and *in vivo* settings. *In vitro* assays mainly capture short-term drug activity, whereas successful systemic therapy requires adequate circulation stability, pathological tissue accumulation, and sustained target engagement [16]. The enhanced tumor retention and prolonged pathway inhibition achieved by PMIProsome therefore provided a critical advantage by maintaining sustained suppression of PAM signaling during disease progression. These findings underscore that, for pathway-targeted therapeutics, optimized exposure kinetics and durable target engagement may be more clinically relevant than maximizing short-term cytotoxic potency. The improved therapeutic performance of PMIProsome therefore arose not from stronger intrinsic activity of PF, but from the ability of the delivery system to optimize drug exposure profiles *in vivo*.

Beyond improving tumor drug delivery, our findings reveal the broader therapeutic potential of controlled PAM modulation in transplantation-associated malignancies. This signaling network integrates proliferative, metabolic, and survival cues that are fundamental to both tumor progression and immune-cell activation [51]. Accordingly, simultaneous regulation of malignant cells and alloimmune responses may be achievable when pathway inhibition is appropriately controlled *in vivo*. In the present study, sustained PAM pathway suppression by PMIProsome was associated with reduced tumor growth, attenuated T-cell activation, decreased dendritic-cell maturation, and prolonged graft survival. These findings suggest that tumor recurrence and alloimmune injury, although clinically distinct processes, may share actionable regulatory nodes that can be modulated through controlled drug delivery. The PMIProsome platform provides an alternative framework in which a single molecular pathway can be systemically regulated while achieving therapeutic effects across distinct pathological contexts. Although further optimization and validation are required, this strategy illustrates how controlled drug delivery can expand the therapeutic applications of existing small-molecule inhibitors in complex disease settings.

Several limitations of the present study should be acknowledged. First, although the orthotopic HCC and transplantation models used herein capture key aspects of tumor progression and alloimmune activation, they do not fully recapitulate the complexity of long-term clinical trajectories after transplantation. In particular, chronic disease evolution and late recurrence patterns remain to be further evaluated in more clinically representative models. Second, the current skin allograft model does not represent the full physiological and immunological environment of solid organ transplantation, and therefore may not entirely reflect long-term allograft responses in a clinical setting. Third, while the current findings highlight coordinated regulation of tumor and immune responses associated with PAM pathway modulation, a more comprehensive characterization of downstream cellular and molecular heterogeneity would further strengthen the mechanistic understanding. Fourth, although the present study demonstrates improved therapeutic outcomes with PMIProsome-based delivery, detailed pharmacokinetics across different physiological compartments was not fully explored. Future studies may focus on further validating this coordinated therapeutic strategy in more clinically relevant transplantation settings and on refining the mechanistic understanding of how tumor and immune processes are jointly regulated. These investigations will be important for translating delivery-controlled PI3K/mTOR inhibition toward clinical applications in transplant oncology.

Overall, this study establishes a prodrug-engineered nanotherapeutic strategy for harnessing dual PI3K/mTOR inhibition in settings where sustained pathway regulation and immune tolerance are simultaneously required. By integrating prodrug engineering with responsive nanoliposomal delivery, PMIProsome improved drug exposure, mitigated systemic toxicity, and enabled coordinated control of tumor progression and alloimmune activation. More broadly, this work highlights the potential of rational delivery design to transform the therapeutic behavior of existing molecular inhibitors and broaden their applications in complex clinical contexts.

Acknowledgements

We thank the excellent technical support (HPLC: Pengda Zou) by the core facility, Central Laboratory, the First Affiliated Hospital, Zhejiang University School of Medicine with the mass spectrometry. We appreciate Zhongyao Gao from Universal Biotech Company, Shanghai, for his assistance with cytometry analysis. We thank Yinping Lv in the Center of Cryo-Electron Microscopy, Zhejiang University for her assistance on TEM.

Funding: This work was supported by Natural Science Foundation of Zhejiang Province (LQN25H160037), "Pioneer" and "Leading Goose" R&D Program of Zhejiang (No. 2025C04007).

Author contributions:

Conceptualization: X.H.Y., Y.Z.T., and Z.S.S.
Methodology: W.N. T.H., and F.Y.
Investigation: F.Y., W.Z.H., and T.X.Y.
Resources: X.H.Y., Z.K., Z.W.T., and Y.Z.T.
Funding acquisition: X.H.Y., Y.Z.T., and Z.S.S.
Data curation: T.H., Z.J.T., and L.Z.
Validation: Z.J.T., S.R.Q., and S.R
Formal analysis: Z.J.T., W.J.M. and S.R.
Supervision: X.H.Y. and Hyon-Seung Yi
Project administration: X.H.Y. and Z.S.S.
Visualization: W.N. and T.X.Y.
Writing-original draft: W.N., and F.Y.

Competing interests: The authors declare no potential competing interests.

Data and materials availability: All data needed to evaluate the conclusions in the paper are present in the paper and/or the Supplementary Materials.

Reference

[1] Li, M., Bhoori, S., Mehta, N., and Mazzaferro, V. (2024) Immunotherapy for hepatocellular carcinoma: The next evolution in expanding access to liver transplantation, *J Hepatol 81*, 743-755.

[2] Yamada, T., Tateishi, R., and Fujishiro, M. (2026) Post-transplant hepatocellular carcinoma: balancing immunosuppression and immune checkpoint inhibitors, *Clin Mol Hepatol 32*, 580-598.

[3] Poudel, K., Vithiananthan, T., Kim, J. O., and Tsao, H. (2025) Recent progress in cancer vaccines and nanovaccines, *Biomaterials 314*, 122856.

[4] Verna, E. C., Patel, Y. A., Aggarwal, A., Desai, A. P., Frenette, C., Pillai, A. A., Salgia, R., Seetharam, A., Sharma, P., Sherman, C., Tsoulfas, G., and Yao, F. Y. (2020) Liver transplantation for hepatocellular carcinoma: Management after the transplant, *Am J Transplant 20*, 333-347.

[5] Kong, L., Xu, K., Bao, X., Ye, K., Fan, D., Wang, N., Deng, Y., Wang, W., Wei, S., and Zhou, L. (2025) mTORC1 Selective Nano-Inhibitor by Disrupting the Lysosomal Arginine-SLC38A9- mTORC1-CDKs Axis for Precision Bladder Cancer Therapy, *Adv Mater 37*, e2504798.

[6] Liu, J., Jiang, B., Xu, W., Liu, Q., Huang, H., Chang, X., Ma, G., Xu, X., Zhou, L., Xiao, G. G., and Guo, J. (2024) Targeted inhibition of CHKalpha and mTOR in models of pancreatic ductal adenocarcinoma: A novel regimen for metastasis, *Cancer Lett 605*, 217280.

[7] Sun, R., Liang, Z., Wang, N., Chen, X., Zhao, J., Tang, H., Zhao, W., Wang, H., Zheng, S., Song, P., and Xie, H. (2025) Advancing immunomodulation in organ transplantation: the therapeutic potential of self-assembled rapamycin nanoparticles in allograft rejection, *J Nanobiotechnology 23*, 418.

[8] Xia, L., Nie, T., Lu, F., Huang, L., Shi, X., Ren, D., Lu, J., Li, X., Xu, T., Cui, B., Wang, Q., Gao, G., and Yang, Q. (2024) Direct regulation of FNIP1 and FNIP2 by MEF2 sustains MTORC1 activation and tumor progression in pancreatic cancer, *Autophagy 20*, 505-524.

[9] Wang, N., Zhou, K., Liang, Z., Sun, R., Tang, H., Yang, Z., Zhao, W., Peng, Y., Song, P., Zheng, S., and Xie, H. (2023) RapaLink-1 outperforms rapamycin in alleviating allogeneic graft rejection by inhibiting the mTORC1-4E-BP1 pathway in mice, *Int Immunopharmacol 125*, 111172.

[10] Dual PI3K/mTOR inhibition is required to combat resistance to CDK4/6 inhibitor and endocrine therapy in PIK3CA- mutant breast cancer, *Science Translational Medicine*.

[11] Wang, H., Huang, F., Zhang, Z., Wang, P., Luo, Y., Li, H., Li, N., Wang, J., Zhou, J., Wang, Y., and Li, S. (2019) Feedback Activation of SGK3 and AKT Contributes to Rapamycin Resistance by Reactivating mTORC1/4EBP1 Axis via TSC2 in Breast Cancer, *Int J Biol Sci 15*, 929-941.

[12] Combined targeting of AKT and mTOR synergistically inhibits proliferation of hepatocellular carcinoma cells, *Molecular Cancer*.

[13] Taylor, M. S., Chen, M., Hancock, M., Wranik, M., Miller, B. D., O'Meara, T. R., Palanski, B. A., Ficarro, S. B., Groendyke, B. J., Xiang, Y., Kondo, K. T., Linde-Garelli, K. Y., Lee, M. J., Mondal, D., Freund, D., Congreve, S., Matas, K., Hennink, M., Xibinaku, K., Valenstein, M. L., van Eeuwen, T., Marto, J. A., Sali, A., Shi, Y., Gray, N. S., Sabatini, D. M., Chu, N., Rogala, K. B., and Cole, P. A. (2026) Structural basis for the recruitment and selective phosphorylation of Akt by mTORC2, *Science 391*, eadv7111.

[14] Ou, X., Tan, Y., Xie, J., Yuan, J., Deng, X., Shao, R., Song, C., Cao, X., Xie, X., He, R., Li, Y., and Tang, H. (2024) Methylation of GPRC5A promotes liver metastasis and docetaxel resistance through activating mTOR signaling pathway in triple negative breast cancer, *Drug Resist Updat 73*, 101063.

[15] Cao, J., Zeng, K., Chen, Q., Yang, T., Lu, F., Lin, C., Zhan, J., Ma, W., Zhou, T., Huang, Y., Luo, F.,

and Zhao, H. (2024) PQR309, a dual PI3K/mTOR inhibitor, synergizes with gemcitabine by impairing the GSK-3beta and STAT3/HSP60 signaling pathways to treat nasopharyngeal carcinoma, *Cell Death Dis 15*, 237.

[16] Yin, L., Yang, F., Wang, W., Zhang, L., Cao, Z., Shi, H., Pan, K., Wu, L., Xiao, H., and Xing, N. (2025) PSMA-Targeted Nanoparticles with PI3K/mTOR Dual Inhibitor Downregulate P-Glycoprotein and Inactivate Myeloid-Derived Suppressor Cells for Enhanced Chemotherapy and Immunotherapy in Prostate Cancer, *Adv Mater 37*, e2415322.

[17] Wesolowski, R., Rugo, H. S., Specht, J. M., Han, H. S., Kabos, P., Vaishampayan, U., Wander, S. A., Gogineni, K., Spira, A., Schott, A. F., Abu-Khalaf, M., Mutka, S. C., Suzuki, S., Sullivan, B., Gorbatchevsky, I., and Layman, R. M. (2025) Gedatolisib Combined with Palbociclib and Letrozole in Patients with No Prior Systemic Therapy for Hormone Receptor-Positive, HER2-Negative Advanced Breast Cancer, *Clin Cancer Res 31*, 4040-4048.

[18] Brown, J. R., Hamadani, M., Hayslip, J., Janssens, A., Wagner-Johnston, N., Ottmann, O., Arnason, J., Tilly, H., Millenson, M., Offner, F., Gabrail, N. Y., Ganguly, S., Ailawadhi, S., Kasar, S., Kater, A. P., Doorduijn, J. K., Gao, L., Lager, J. J., Wu, B., Egile, C., and Kersten, M. J. (2018) Voxtalisib (XL765) in patients with relapsed or refractory non-Hodgkin lymphoma or chronic lymphocytic leukaemia: an open-label, phase 2 trial, *Lancet Haematol 5*, e170-e180.

[19] Bhat, M., Usmani, S. E., Azhie, A., and Woo, M. (2021) Metabolic Consequences of Solid Organ Transplantation, *Endocr Rev 42*, 171-197.

[20] Higdon, L. E., Tan, J. C., and Maltzman, J. S. (2023) Infection, Rejection, and the Connection, *Transplantation 107*, 584-595.

[21] Yang, Q., Ma, X., Xiao, Y., Zhang, T., Yang, L., Yang, S., Liang, M., Wang, S., Wu, Z., Xu, Z., and Sun, Z. (2022) Engineering prodrug nanomicelles as pyroptosis inducer for codelivery of PI3K/mTOR and CDK inhibitors to enhance antitumor immunity, *Acta Pharm Sin B 12*, 3139-3155.

[22] Burke, J. A., Zhang, X., Bobbala, S., Frey, M. A., Bohorquez Fuentes, C., Freire Haddad, H., Allen, S. D., Richardson, R. A. K., Ameer, G. A., and Scott, E. A. (2022) Subcutaneous nanotherapy repurposes the immunosuppressive mechanism of rapamycin to enhance allogeneic islet graft viability, *Nat Nanotechnol 17*, 319-330.

[23] Chen, X., Meng, F., Xu, Y., Li, T., Chen, X., and Wang, H. (2023) Chemically programmed STING-activating nano-liposomal vesicles improve anticancer immunity, *Nat Commun 14*, 4584.

[24] Lim, H., Moon, Y., Han, S., Cho, H., Song, S., Kim, J., Goo, J., Shim, N., Guo, L., Kim, T. I., Chang, W. S., Koh, W. G., and Kim, K. (2026) Low-dose radiation generated ROS-activatable doxorubicin prodrug loaded liposome nanoparticles for triple-negative breast cancer treatment, *J Control Release 393*, 114750.

[25] Jiang, Y., Chen, H., Lin, T., Zhang, C., Shen, J., Chen, J., Zhao, Y., Xu, W., Wang, G., and Huang, P. (2024) Ultrasound-activated prodrug-loaded liposome for efficient cancer targeting therapy without chemotherapy-induced side effects, *J Nanobiotechnology 22*, 2.

[26] Liu, Y., Wang, X., Xu, H., Wu, H., Ju, Y., Cui, L., Zhao, Y., Chen, Y., Cui, M., and Yang, F. (2025) Ultrasound-Visualized Cuproptosis in Glioblastoma via Endogenous Copper Sequestration and Nitric Oxide-Gas Controlled Release Using a Programmable Nanoliposomal Platform, *ACS Nano 19*, 38594-38613.

[27] Yang, Z., Xie, H., Wan, J., Wang, Y., Zhang, L., Zhou, K., Tang, H., Zhao, W., Wang, H., Song, P.,

and Zheng, S. (2023) A nanotherapeutic strategy that engages cytotoxic and immunosuppressive activities for the treatment of cancer recurrence following organ transplantation, *EBioMedicine 92*, 104594.

[28] Xu, W., Berning, P., Erdmann, T., Grau, M., Bettazova, N., Zapukhlyak, M., Frontzek, F., Kosnopfel, C., Lenz, P., Grondine, M., Willis, B., Lynch, J. T., Klener, P., Hailfinger, S., Barry, S. T., and Lenz, G. (2023) mTOR inhibition amplifies the anti-lymphoma effect of PI3Kbeta/delta blockage in diffuse large B-cell lymphoma, *Leukemia 37*, 178-189.

[29] Guan, Y., Jiang, S., Ye, W., Ren, X., Wang, X., Zhang, Y., Yin, M., Wang, K., Tao, Y., Yang, J., Cao, D., and Cheng, Y. (2020) Combined treatment of mitoxantrone sensitizes breast cancer cells to rapalogs through blocking eEF-2K-mediated activation of Akt and autophagy, *Cell Death Dis 11*, 948.

[30] Marui, T., Fukahori, H., Ito, M., Kaneko, Y., Maeda, M., Tsujimoto, S., and Morokata, T. (2019) The PI3Kdelta selective inhibitor AS2541019 suppresses donor-specific antibody production in rat cardiac and non-human primate renal allotransplant models, *Int Immunopharmacol 75*, 105756.

[31] Sang, A. X., McPherson, M. C., Ivison, G. T., Qu, X., Rigdon, J., Esquivel, C. O., Krams, S. M., and Martinez, O. M. (2019) Dual blockade of the PI3K/Akt/mTOR pathway inhibits posttransplant Epstein-Barr virus B cell lymphomas and promotes allograft survival, *Am J Transplant 19*, 1305-1314.

[32] Li, W., Yu, C., Zhang, X., Gu, Y., He, X., Xu, R., Xu, J., Yu, G., and Wu, Y. (2025) Dendritic cells: understanding ontogeny, subsets, functions, and their clinical applications, *Mol Biomed 6*, 62.

[33] Sen, K., Pati, R., Jha, A., Mishra, G. P., Prusty, S., Chaudhary, S., Swetalika, S., Podder, S., Sen, A., Swain, M., Nanda, R. K., and Raghav, S. K. (2023) NCoR1 controls immune tolerance in conventional dendritic cells by fine-tuning glycolysis and fatty acid oxidation, *Redox Biol 59*, 102575.

[34] Yu, L., Wei, J., and Liu, P. (2022) Attacking the PI3K/Akt/mTOR signaling pathway for targeted therapeutic treatment in human cancer, *Semin Cancer Biol 85*, 69-94.

[35] Zhou, K., Chen, X., Zhang, L., Yang, Z., Zhu, H., Guo, D., Su, R., Chen, H., Li, H., Song, P., Xu, X., Wang, H., Zheng, S., and Xie, H. (2021) Targeting peripheral immune organs with self-assembling prodrug nanoparticles ameliorates allogeneic heart transplant rejection, *Am J Transplant 21*, 3871-3882.

[36] Wang, M., Zhang, Q., Wang, Y., Sun, Y., Zhang, N., Liu, M., Meng, H., Li, Y., Wang, X., Zhang, L., and Bachert, C. (2026) IL-2 synergizes with proinflammatory type 3 inducers to amplify mixed type 2-type 3 inflammation in nasal polyps, *J Allergy Clin Immunol 157*, 1071-1086.

[37] European Association for the Study of the, L. (2025) EASL Clinical Practice Guidelines on the management of hepatocellular carcinoma, *J Hepatol 82*, 315-374.

[38] Tabrizian, P., Abdelrahim, M., and Schwartz, M. (2024) Immunotherapy and transplantation for hepatocellular carcinoma, *J Hepatol 80*, 822-825.

[39] Sha, M., Wang, J., Cao, J., Zou, Z. H., Qu, X. Y., Xi, Z. F., Shen, C., Tong, Y., Zhang, J. J., Jeong, S., and Xia, Q. (2025) Criteria and prognostic models for patients with hepatocellular carcinoma undergoing liver transplantation, *Clin Mol Hepatol 31*, S285-S300.

[40] Broering, D. C., Marcos, A., Abreu, P., Raptis, D. A., Alnemary, Y., Malago, M., and Elsheikh, Y. (2025) Establishment and standardization of a robotic donor hepatectomy technique for

liver transplantation: a pure surgical approach based on 1400 cases, *Int J Surg*.

[41] Li, Z., Taner, T., Eaton, J. E., Smith, B. H., Ilyas, S. I., Hallemeier, C. L., Tran, N. H., Diwan, T. S., Mathur, A. K., Lizaola-Mayo, B. C., Perry, D. K., Yang, L., Gores, G. J., and Heimbach, J. K. (2025) Development of the Perihilar Cholangiocarcinoma Risk Estimation of Tumor Recurrence After Transplant (PRETREAT) Score, *Ann Surg 282*, 503-514.

[42] Li, P. J., Tabrizian, P., Daher, D., Gaviria, F., Ajmera, V., Montalvan-Sanchez, E. E., Gutierrez, J. A., Zhou, K., Delebecque, F., Garcia, N., Barrick, B., Wong, C., Nephew, L., Holden, J., Dave, S., Schnickel, G. T., Rich, N. E., Florman, S. S., Sapisochin, G., Yao, F., Singal, A. G., and Mehta, N. (2025) A prospective multicenter validation of RETREAT for posttransplantation HCC recurrence prediction, *Hepatology 82*, 1450-1460.

[43] Chen, J., Li, H., Zhuo, J., Lin, Z., Hu, Z., He, C., Wu, X., Jin, Y., Lin, Z., Su, R., Sun, Y., Wang, R., Sun, J., Wei, X., Zheng, S., Lu, D., and Xu, X. (2024) Impact of immunosuppressants on tumor pulmonary metastasis: new insight into transplantation for hepatocellular carcinoma, *Cancer Biol Med 21*, 1033-1049.

[44] Kim, S. Y., Jo, M. J., Yoon, M. S., Jin, C. E., Shin, Y. B., Lee, J. M., Shin, H. J., Oh, J. G., Cho, J. M., Kim, H., Park, H., Choi, Y. W., Park, C. W., Kim, J. S., and Shin, D. H. (2023) Gemcitabine and rapamycin-loaded mixed polymeric thermogel for metastatic pancreatic cancer therapy, *J Control Release 360*, 796-809.

[45] Krynychka, K., Katz-Greenberg, G., Byrns, J. S., Shaw, B. I., Bhavsar, N. A., Rogers, U., Jackson, A. M., Ellis, M. J., Luo, X., and Kirk, A. D. (2026) Off-label use of alemtuzumab, belatacept, and rapamycin in kidney transplantation-Long-term real-world experience, *Am J Transplant 26*, 140-150.

[46] Lactobacillus rhamnosus HN001 facilitates the efficacy of dual PI3K/mTOR inhibition prolonging cardiac transplant survival and enhancing antitumor effect, *Microbial Pathogenesis*.

[47] Rubinstein, M. M., Hyman, D. M., Caird, I., Won, H., Soldan, K., Seier, K., Iasonos, A., Tew, W. P., O'Cearbhaill, R. E., Grisham, R. N., Hensley, M. L., Troso-Sandoval, T., Sabbatini, P., Guillen, J., Selcuklu, S. D., Zimel, C., Torrisi, J., Aghajanian, C., and Makker, V. (2020) Phase 2 study of LY3023414 in patients with advanced endometrial cancer harboring activating mutations in the PI3K pathway, *Cancer 126*, 1274-1282.

[48] Wu, X., Xu, Y., Liang, Q., Yang, X., Huang, J., Wang, J., Zhang, H., and Shi, J. (2022) Recent Advances in Dual PI3K/mTOR Inhibitors for Tumour Treatment, *Front Pharmacol 13*, 875372.

[49] Huang, W. K., Chen, Y., Su, H., Chen, T. Y., Gao, J., Liu, Y., Yeh, C. N., and Li, S. (2021) ARHGAP25 Inhibits Pancreatic Adenocarcinoma Growth by Suppressing Glycolysis via AKT/mTOR Pathway, *Int J Biol Sci 17*, 1808-1820.

[50] Raza, F., Evans, L., Motallebi, M., Zafar, H., Pereira-Silva, M., Saleem, K., Peixoto, D., Rahdar, A., Sharifi, E., Veiga, F., Hoskins, C., and Paiva-Santos, A. C. (2023) Liposome-based diagnostic and therapeutic applications for pancreatic cancer, *Acta Biomater 157*, 1-23.

[51] Zhao, J., Zhang, Y., Wei, Z., Li, K., Sun, L., Li, D., and Wang, Y. (2025) The PI3K/Akt/mTOR Pathway: Immuno-Metabolic Orchestration in IR/MASH-Associated Hepatocellular Carcinoma, *Int J Biol Sci 21*, 6025-6041.

Supplementary Files

This is a list of supplementary files associated with this preprint. Click to download.

- Supplementarymaterial.docx
- WesternBlot.pdf